Observation of electrochemical capacitance in a graphite surface by noncontact scanning nonlinear dielectric microscopy

Shin-ichiro Kobayashi* and Yasuo Cho
Research Institute of Electrical Communication, Tohoku University, 2-1-1 Katahira, Aoba-ku, Sendai 980-8577, Japan
(Received 1 June 2010; revised manuscript received 30 September 2010; published 30 December 2010)

We have developed a noncontact, scanning nonlinear dielectric microscopy (NC-SNDM) system operated under ultrahigh vacuum and have used it to observe the surface of graphite. By using the NC-SNDM technique (2ω amplitude feedback mode), we succeeded in obtaining clear SNDM images of the graphite surface. In the SNDM image patterns (inverted contrast ω amplitude image), a number of convex spots, with threefold symmetry, positioned at the corners of hexagons were observed when the probe tip was near the graphite surface. In contrast, a number of convex spots, with threefold symmetry, were also observed in the normal contrast ω amplitude image when the distance between the probe tip and graphite was large. Current images originating from tunneling were also observed in NC-SNDM and were similar to the ω amplitude images. Electrochemical capacitance between the probe tip and graphite surface with tunneling was introduced to investigate the origin of the SNDM signal. Applying this model to the NC-SNDM measurement, we found that the ω amplitude signal is dependent on the ratio of the slope of the local density of states (LDOS) and the energy curve, and the LDOS at the Fermi energy in the graphite surface. The convex spots and hollow spots in the hexagons on the graphite surface also originate from the LDOS in the NC-SNDM measurements. This means that the SNDM signal for the graphite surface reflects the LDOS on the graphite surface. Considering the relationship between the ω amplitude signal and LDOS on the graphite surface, the current signal observed in the NC-SNDM measurement originates from the tunneling effect between the probe tip and graphite surface. The proposed technique can potentially detect not only a unique carbon surface but also organic molecules on a metallic surface.

DOI: 10.1103/PhysRevB.82.245427 PACS number(s): 68.37.−d, 73.20.At, 73.30.+y

I. INTRODUCTION

A new and promising technique, "scanning nonlinear dielectric microscopy" (SNDM), was recently introduced.[1–7] The SNDM technique has high sensitivity to variations in the capacitance, on the order of 10^{-22} F and we were indirectly able to use it to visualize electron and hole distributions in semiconductor flash memory devices.[8–10] The resolution of the SNDM technique in contact mode operation is in the subnanometer order for the measurement of ferroelectric domains and charge distributions in a semiconductor device. In contrast, Hirose *et al.* have recently developed noncontact SNDM (NC-SNDM), and have used this to visualize the topography as well as the microscopic electric dipole moment distribution induced by one adatom and three Si atoms below this adatom on a Si(111)-7×7 reconstructed structure.[11–14] Thus, NC-SNDM is a powerful technique to evaluate a surface with microscopic electric dipole moments without damaging the surface of the specimen.

Graphite is a stable-carbon material with a layered structure including a number of carbon sheets comprised of a honeycomb structure made up of sp^2 carbon atoms. Each layer of graphite corresponds to "*graphene*" which has recently been attracting much attention.[15–18] The individual sheets are strongly bonded by Van der Waals interactions. A schematic representation of the structure of a bulk graphite crystal is shown in Fig. 1, indicating two nonequivalent types of carbon-atom sites. The *A*-site carbon in hexagonal graphite (with *ABAB* stacking) has a neighbor directly below in the second layer whereas the *B*-site carbon is located above the center of a hexagon of the layer beneath. Thus, differences in the local density of states (LDOS) occur for the two sites as a consequence of this carbon-site asymmetry and interlayer interactions.

This difference in the LDOS in graphite has been reported in previous scanning tunnel microscope (STM) measurements.[19,20] Images of graphite observed by STM show complicated, varying patterns.[20–23] One frequently seen pattern is a hollow with convex spots with threefold symmetry.[20,21,23] A striped pattern is also observed due to the condition of the probe tip.[21,22] The most attractive pattern is a clear honeycomb structure recognized in the inverted contrast images.[23] In addition to the honeycomb structure, the heights at alternating three carbon atoms (*A* sites) in the hexagon are larger than those at the other three carbon atoms (*B* sites). This is due to the difference in LDOS between the *A* and *B* sites. For this reason, images reflecting the LDOS in the graphite surface were observed in the STM measurements.

In this paper, we present SNDM images of the well-known graphite [highly oriented pyrolytic graphite (HOPG)] surface by using the NC-SNDM technique under ultrahigh vacuum. In the following sections, the principle of NC-SNDM is described. In Sec. III, the experimental methods used are described. In Sec. IV, we show the topographies, SNDM images and current images of the graphite surface as well as the approach curve of the Au(111) surface obtained in this study. Section IV is devoted to a discussion on the origin of SNDM images for a graphite surface using model calculations.

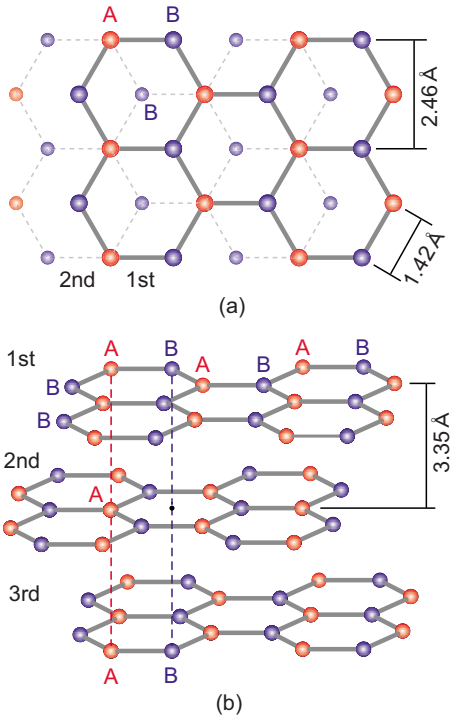

FIG. 1. (Color online) Schematic of three successive layers of hexagonal graphite in (a) top view and (b) side view. The two nonequivalent types of carbon atom sites are shown: *A* types have neighbors directly below in the second layer and *B*-types are located above a hexagon. The in-layer nearest carbon-carbon distance is 1.42 Å and the carbon layers are separated by 3.35 Å.

II. PRINCIPLE

A. Principle of NC-SNDM

A system diagram of the NC-SNDM apparatus is shown in Fig. 2(a). The metal probe is connected to the inductance (L) and capacitance (C) resonance circuit in a voltage-control oscillator, and the resonance angular frequency is defined as $\Omega_r = 1/\sqrt{LC}$. The total capacitance (C_t) between the tip and the return ring is written as $C_t(d) = [1/C_{S\text{-}R}(d) + 1/C_{S\text{-}P}(d) + 1/C_{tip} + 1/C_s]^{-1} + C_{P\text{-}R}$, as shown in Fig. 2(b). Here, d, $C_{P\text{-}R}$, $C_{S\text{-}R}(d)$, $C_{S\text{-}P}(d)$, C_{tip}, and C_s are expressed as the distance between the probe tip and surface of the specimen, the capacitance between the probe and return ring, the capacitance between the surface of the specimen and the return ring, the capacitance between the probe tip and the specimen surface, the capacitance originating from the electrical properties of the probe tip, and the capacitance originating from the electrical properties of the specimen, respectively. Considering that the area of the return ring and the distance between the return ring and specimen surface are ~ 10 mm^2 and ~ 1 mm, respectively, and the area and gap between the probe tip and the surface in the NC-SNDM measurement are ~ 100 nm^2 and ~ 1 nm, respectively, we can obtain $C_{S\text{-}R}(d) \gg [1/C_s + 1/C_{S\text{-}P}(d)]^{-1}$. As a result, $C_{S\text{-}R}$ is neglected in $C_t(d)$ as shown in Fig. 2(c), and C_t is expressed as $C_t(d) \simeq C(d) + C_{P\text{-}R}$ where

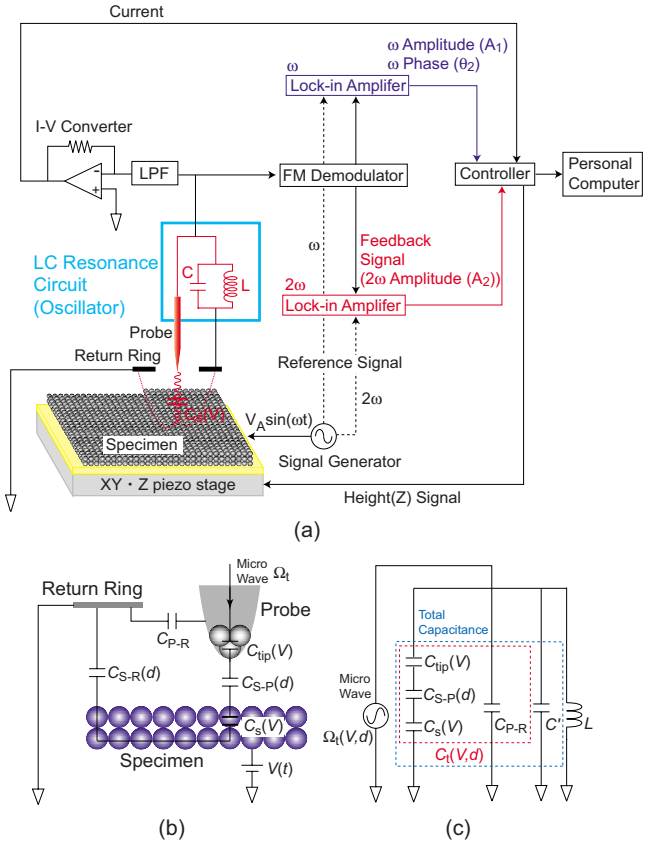

FIG. 2. (Color online) (a) Schematic of the NC-SNDM apparatus. The NC-SNDM technique utilizes the 2ω amplitude signal as a feedback signal for maintaining the gap between the tip and the specimen. The topographical and ω amplitude (variation in the capacitance) and phase (sign of the slope of the capacitance-voltage curve) images were observed simultaneously for the same scanned area. In this study, the amplitude and frequency of the applied alternating voltage were 30 kHz and 0.4 $V_{p\text{-}p}$, respectively. (b) The equivalent circuit between the probe and return ring. $C_{P\text{-}R}$, $C_{S\text{-}R}(d)$, $C_{S\text{-}P}(d)$, C_{tip}, and C_s are the capacitance between the probe and the return ring, the capacitance between the specimen surface and return ring, the capacitance between the probe tip and specimen surface, the capacitance originating from the surface structure of the probe tip, and the capacitance originating from the surface structure of the specimen, respectively. (c) The final equivalent circuit between the probe and return ring. $C_t \simeq [1/C_{tip} + 1/C_s + 1/C_{tip} + 1/C_{S\text{-}P}(d)]^{-1} + C_{P\text{-}R}$ because of large $C_{S\text{-}R}(d)$.

$$C(d) \equiv \left[\frac{1}{C_s} + \frac{1}{C_{tip}} + \frac{1}{C_{S\text{-}P}(d)} \right]^{-1} \tag{1}$$

and is the capacitance originating from the electrical properties of the probe tip and the surface of the specimen, and the gap between the probe tip and the surface of the specimen. Therefore, the measured resonance angular frequency is

$$\Omega_t(d) = \frac{1}{\sqrt{L[C' + C_t(d)]}} = \frac{1}{\sqrt{L[C' + C_{P\text{-}R} + C(d)]}}, \tag{2}$$

where C' is the stray capacitance in the oscillator circuit. Here, it is to be noted that an understanding of the origins of C_{tip} and C_s is the most important in this study. For this rea-

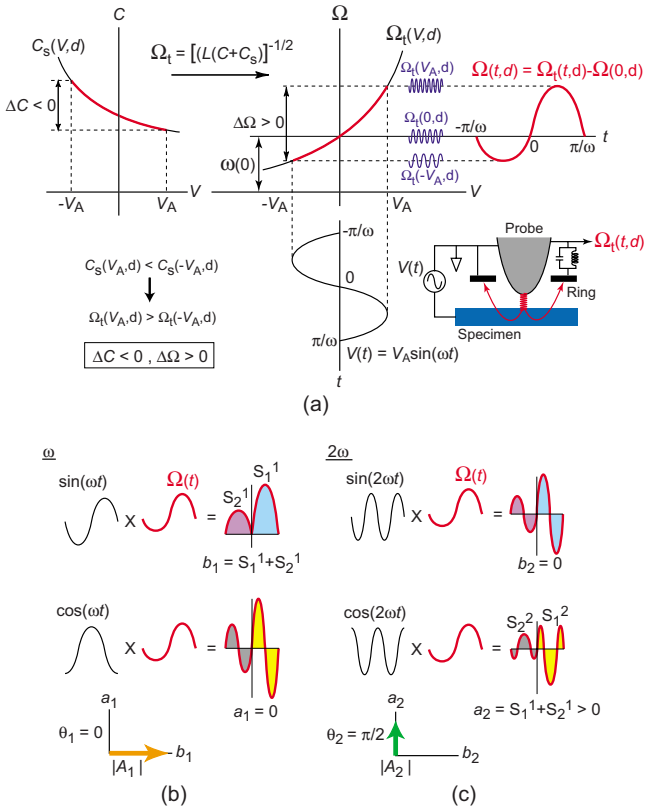

FIG. 3. (Color online) (a) The relationship between the applied alternating voltage $V(t)$ and the response function modulated by the capacitance which depends on the applied voltage. The modulated frequency $\Omega_t(d)$ is expressed as $\Omega_t(d)=[C+C_t(V,d)]^{-1/2}$ for d. Since the $\Omega_t(V)$ curve is nonlinear, $\Omega_t(t,d)$ or $\Omega(t,d)[\equiv\Omega_t(t,d)-\Omega(0,d)]$ is a complicated curve and includes in not only the ω component but also the 2ω component, the 3ω component, etc. (b) Computational method of the amplitude and phase for the ω component. For computing the ω component, we need to integrate $\Omega(t,d)\sin(\omega t)$ or $\Omega(t,d)\cos(\omega t)$ between $-\pi/\omega$ and π/ω. Since $\Omega(t,d)\sin(\omega t)$ is asymmetrical around $t=\pm\pi/2\omega$, the integration of $\Omega(t,d)\sin(\omega t)$ is finite. On the other hand, the integration of $\Omega(t,d)\cos(\omega t)$ is zero because $\Omega(t,d)\cos(\omega t)$ is symmetrical around $t=\pm\pi/2\omega$. The amplitude $A_1(d)$ and phase $\theta_1(d)$ are easily obtained from Eq. (13) in the principle of NC-SNDM. (c) Computational method of the amplitude and phase for the 2ω component. By similar computation as the ω component, $A_2(d)$ and $\theta_2(d)$ are easily obtained.

son, the origins of these capacitances will be discussed later.

If C_{tip} or C_s or both C_{tip} and C_s depend on the applied voltage (V), the resonance angular frequency $[\Omega_t(d)]$ also depends on V, and therefore

$$\Omega_t(V,d)=\frac{1}{\sqrt{L[C'+C_{P\text{-}R}+C(V,d)]}}. \tag{3}$$

Since an alternating voltage $[V(t)=V_A\sin(\omega t)]$ is applied between the probe tip and the lower electrode, $\Omega_t(V,d)$ also depends on the time (t) as seen in Fig. 3(a). Accordingly

$$\Omega_t(t,d)=\Omega_t[V(t),d]=\frac{1}{\sqrt{L\{C'+C_{P\text{-}R}+C[V_A\sin(\omega t),d]\}}}. \tag{4}$$

Equation (4) is a periodic function between $-\pi/\omega$ and π/ω and can be expanded by the basis functions $[\cos(m\omega t)$ and $\sin(m\omega t)$, $m=1,2,3,\ldots]$. These yield

$$\Omega_t(t,d)=\Omega_0(d)+\sum_{m=1}^{\infty}[a_m(d)\cos(m\omega t)+b_m(d)\sin(m\omega t)], \tag{5}$$

where

$$\Omega_0(d)\equiv\frac{\omega}{2\pi}\int_{-\pi/\omega}^{\pi/\omega}\Omega_t(t,d)dt=\Omega_t(0,d)+\frac{\omega}{2\pi}\int_{-\pi/\omega}^{\pi/\omega}\Omega(t,d)dt, \tag{6}$$

$$a_m(d)\equiv\frac{\omega}{\pi}\int_{-\pi/\omega}^{\pi/\omega}\Omega_t(t,d)\cos(m\omega t)dt=\frac{\omega}{\pi}\int_{-\pi/\omega}^{\pi/\omega}\Omega(t,d)\cos(m\omega t)dt, \tag{7}$$

$$b_m(d)\equiv\frac{\omega}{\pi}\int_{-\pi/\omega}^{\pi/\omega}\Omega_t(t,d)\sin(m\omega t)dt=\frac{\omega}{\pi}\int_{-\pi/\omega}^{\pi/\omega}\Omega(t,d)\sin(m\omega t)dt, \tag{8}$$

$$\Omega_t(0,d)\equiv\frac{1}{\sqrt{L\{C'+C_{P\text{-}R}+C[V(0),d]\}}}=\frac{1}{\sqrt{L[C'+C_{P\text{-}R}+C(0,d)]}}, \tag{9}$$

$$\Omega(t,d)\equiv\Omega_t(t,d)-\Omega_t(0,d)=\Omega_t(0,d)\sum_{n=0}^{\infty}\frac{(-1)^n}{n!}\left(\prod_{k=0}^{n}\frac{2k+1}{2}\right)\times\left[\frac{\Delta C(t,d)}{C'+C_{P\text{-}R}+C(0,d)}\right]^n \tag{10}$$

$$\Delta C(t,d)\equiv C[V_A\sin(\omega t),d]-C(0,d). \tag{11}$$

Furthermore, using the relationship

$$A_m(d)\equiv\sqrt{[a_m(d)]^2+[b_m(d)]^2}, \tag{12}$$

$$\theta_m(d)\equiv\arctan\left[\frac{a_m(d)}{b_m(d)}\right]. \tag{13}$$

We can easily obtain the amplitude $[A_m(d)]$ and phase $[\theta_m(d)]$ for the mth order and d. $\Omega_0(d)$ in Eq. (5) corresponds to the angular frequency of the carrier in FM. As seen from

Eqs. (7), (8), (10), and (11), $a_m(d)$ and $b_m(d)$ are proportional to ω, $\Omega_t(0,d)$ and $\{\Delta C(t,d)/[C'+C_{P\text{-}R}+C(0,d)]\}^n$, respectively. These parameters need to be as large as possible to obtain high sensitivities of $a_m(d)$ and $b_m(d)$. It is easy to change the amplitude of ω because ω is the angular frequency of the applied alternating voltage. $\Delta C(t,d)$ strongly depends on V_A, as seen in Fig. 3(a). Furthermore, to make $\Omega_t(0,d)$ large, the inductance or capacitance in the LC resonance circuit needs to be reduced. If it is difficult to reduce the inductance, C' or $C_{P\text{-}R}$ should be reduced because $C(0,d)$ does not strongly contribute to the resonance frequency in the actual system, as described in Sec. IV C. $C_{P\text{-}R}$ depends on the position of the return ring and probe. On the other hand, C' depends on the circuit in the oscillator. Accordingly, it is necessary to not only devise the settings of the return ring and probe but also to choose an oscillator with a small C'. As a result, the microwave is used as the carrier wave of the FM modulation in the NC-SNDM measurement to obtain high sensitivities of $a_m(d)$ and $b_m(d)$.

The most important component in Eq. (5) is normally the second (ω) component in the SNDM measurement because the ω component is reflected in the polarization of ferroelectrics and the polarity of the semiconductor device.[1–10] Contact mode atomic force microscopy (AFM) is typically used for the SNDM measurements to observe the ω component and the topography of the specimen simultaneously. For this reason, it is necessary to use a cantilever coated with a metal and to connect the cantilever to the oscillator in the SNDM measurement. However, it is difficult to observe the topography by using the SNDM signal in the SNDM measurement due to the large stray capacitance between the cantilever and the surface of the specimen. To resolve this problem, we have proposed the NC-SNDM measurement as shown in Fig. 2(a).[11–14,24,25] In the NC-SNDM measurement, not only the second (ω) but also the third (2ω) component in Eq. (5) is a very important component because the 2ω amplitude signal (A_2) is usually used as the feedback signal to prevent the probe tip from contacting the surface of the specimen.[11–14,24,25] The reason why the 2ω amplitude signal (A_2) is usually used as the feedback signal, as described in the next section. Furthermore, the vertical and lateral resolution of the SNDM signal for the metallic surface in the NC-SNDM measurement can be discussed by considering the origin of the SNDM signal for a metallic surface in the Sec. IV C.

B. Amplitude, phase, and current signals in NC-SNDM

First, we describe the characteristics of the ω and 2ω components for the SNDM signal. In order to understand the characteristics of the ω and 2ω components for d, a_1, b_1 and a_2, b_2 are estimated. The notation d is neglected below since it is an unnecessary parameter to understand the characteristics of the ω and 2ω components. Assuming the $C(V)$ curve as shown in Fig. 3(a), we can obtain the $\Omega(t)$ curve by using Eqs. (3) and (10). First, we calculate the ω component for the $\Omega(t)$ curve in Fig. 3(a). $\Omega(t)\cos(\omega t)$ is asymmetrical around $t=\pm\pi/2\omega$, as seen from Fig. 3(b). In contrast, $\Omega(t)\sin(\omega t)$ is symmetrical around $t=\pm\pi/2\omega$. Accordingly, we easily understand $a_1=0$ and $b_1=S_1^1+S_2^1$, where S_1^1 and S_2^1 denote areas of the right and left sides of $\Omega(t)\sin(\omega t)$. A_1 and θ_1 are obtained from Eq. (13). If $b_1>0$, as shown in Fig. 3(b), A_1 and θ_1 can be estimated as $A_1=b_1$ and $\theta_1=0$. Next, we calculate the 2ω component for the $\Omega(t)$ curve in Fig. 3(a). Similar to the ω component, considering the symmetries of $\Omega(t)\cos(2\omega t)$ and $\Omega(t)\sin(2\omega t)$, we can easily understand $a_2=S_1^2+S_2^2$ and $b_2=0$, where S_1^2 and S_2^2 denote areas of the right and left sides of $\Omega(t)\cos(2\omega t)$. A_2 and θ_2 are obtained

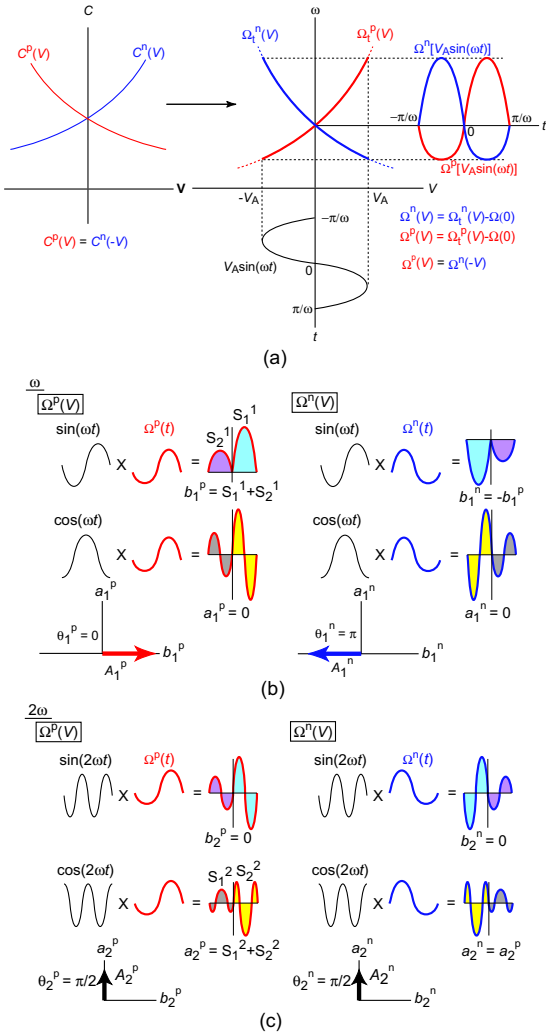

FIG. 4. (Color online) (a) The response functions for two curves for which the sign of the slope is different. Note that the notation of d is neglected due to an unnecessary parameter to understand the characteristics of the ω and 2ω components. The phase is different in $\Omega^n[V_A\sin(\omega t)]$ and $\Omega^p[V_A\sin(\omega t)]$ only by π. (b) The integrations for $\Omega^n[V_A\sin(\omega t)]$, $\Omega^p[V_A\sin(\omega t)]$ and $\Omega^n[V_A\cos(\omega t)]$, $\Omega^p[V_A\cos(\omega t)]$ for the ω component. The phase is different in Ω^n and Ω^p only by π. (c) The integrations for $\Omega^n[V_A\sin(\omega t)]$, $\Omega^p[V_A\sin(\omega t)]$ and $\Omega^n[V_A\cos(\omega t)]$, $\Omega^p[V_A\cos(\omega t)]$ for the 2ω component. Note that phase reversal does not occur for the 2ω component. (d) Variations in the capacitance and resonance frequency for cases 1 $[C_1(V)$ and $\Omega_{t1}(V)]$ and 2 $[C_2(V)$ and $\Omega_{t2}(V)]$ within $\pm V_A$. The magnitude of the variation in the $C_1(V)$ curve is larger than that of the $C_2(V)$ curve within $\pm V_A$. On the other hand, the magnitude of the variation in the $\Omega_{t1}(V)$ curve is smaller than that of the $\Omega_{t2}(V)$ curve within $\pm V_A$ due to Eq. (3).

from Eq. (13). If $a_2>0$, as shown in Fig. 3(c), A_2 and θ_2 can be estimated to be $A_2=a_2$ and $\theta_2=\pi/2$. Thus, A_1, θ_1 and A_2, θ_2 for the optional $C(V)$ curve shown in Fig. 3(a) can be easily calculated from the symmetry of $\Omega(t)\cos(m\omega t)$ or $\Omega(t)\sin(m\omega t)$.

The characteristics of A_1 and A_2 are examined next. First, we consider the relationship between A_1, A_2 and the variation in the $C_s(V)$ curve within $\pm V_A$, as shown in Fig. 3(a). The maximum $[\Omega_t(V_A)]$ and minimum $[\Omega_t(-V_A)]$ of the $\Omega_t(V)$ curve within $\pm V_A$ correspond to the minimum $[C_s(V_A)]$ and maximum $[C_s(-V_A)]$ of the $C_s(V)$ curve within $\pm V_A$. Accordingly, $C_s(V_A)$ and $C_s(-V_A)$ are reflected in the amplitude of the $\Omega_t(t)$ curve. If the variation in the $C_s(V)$ curve within $\pm V_A$ becomes large, A_1 is enhanced because A_1 (b_1) depends on the amplitude of the $\Omega_t(t)$ curve. Thus, A_1 and A_2 are reflected in the variation in the $C_s(V)$ curve within $\pm V_A$. Next, we consider the difference between A_1 and A_2. If V_A is very small, the $\Omega_t(V)$ curve within $\pm V_A$ is assumed to be linear. As seen from Fig. 3(c), $S_1^2=-S_2^2$, and A_2 becomes zero although A_1 is finite as seen from Fig. 3(b). Accordingly, A_2 is zero for small V_A although A_1 is finite as long as C_s depends on V. Thus, A_1 is finite regardless of the curvature of the $\Omega_t(V)$ curve whereas A_2 is reflected in the curvature of the $\Omega_t(V)$ curve.

Next, the characteristics of θ_1 and θ_2 are considered. In order to understand what parameter θ_1 is in the SNDM measurement, we assume two cases (Ω_t^p and Ω_t^n) as shown in Fig. 4(a). To make this problem easier to solve, the absolute value of the slope of the $C_t^p(V)$ curve within $\pm V_A$ is assumed to be the same as that of the $C_t^n(V)$ curve within $\pm V_A$. Here, $C_t^p(V)$ and $C_t^n(V)$ denote the voltage-capacitance curves which lead to Ω_t^p and Ω_t^n. Taking into account the slopes of both the $C_t^p(V)$ and $C_t^n(V)$ curves within $\pm V_A$, it is clear that the phase of $\Omega_t^p(t)$ is different from that of $\Omega_t^n(V)$ by π, as seen from Fig. 4(a). This suggests that phase reversal occurs as the sign of the slope of the capacitance-voltage curve is reversed. To observe the phases for Ω_t^p and Ω_t^n, the NC-SNDM technique utilizes the phase for the ω component. Calculating θ_1^p and θ_1^n by a similar procedure as in Fig. 3(b), we obtain $\theta_1^p=0$ and $\theta_1^n=\pi$ as seen from Fig. 4(b). This indicates that the relationship between θ_1^p and θ_1^n is the same as the relationship between the phase of Ω_t^p and that of Ω_t^n. Consequently, we can indirectly guess the signs of the slopes for the $C_t^p(V)$ and $C_t^n(V)$ curves from the ω phase signal. As an actual example, we consider n- and p-type metal-insulator-semiconductor (MIS) diodes.[10] The slope of the $C(V)$ curves for n-type and p-type MIS diodes are negative and positive in the NC-SNDM measurement. The reason why these slopes are inverted is that the voltage to modulate the capacitance is applied not to the gate electrode but rather to the semiconductor in the MIS diode. Accordingly, the $C(V)$ curves for n- and p-type MIS diodes correspond to the $C^p(V)$ and $C^n(V)$ curves in Fig. 4(b). The ω phase is π for the p-type MIS diode, while it is 0 for the n-type MIS diode, as seen from Fig. 4(b). Thus, to investigate the ω phase signal, one needs to know the sign of the slope of the $C(V)$ curve of the specimen. Actually, the change in phase from 0 to π, i.e., phase reversal in the ω phase signal, was observed in the p- and n-type MIS diodes by contact mode SNDM measurements. On the other hand, we can explain the characteristics of θ_2 although θ_2 is not more important than θ_1. Similar to the calculation for the phase for the ω component, we can calculate the phases for the 2ω component obtained from Ω_t^p and Ω_t^n. The absolute value of the slope of the $C_t^p(V)$ curve is assumed to be the same as that of the $C_t^n(V)$ curve. Calculating θ_2^p and θ_2^n, as shown in Fig. 4(c), we obtain $a_2^p=a_2^n=A_2$ and $b_2^p=0$, $b_2^n=0$. Consequently, $\theta_2^p=\theta_2^n$. This suggests that phase reversal does not occur for the 2ω phase. Hence, we cannot use the phase of the 2ω component to observe phase reversal such as electric polarization.[1–14,24,25]

The signals for $m=3$ or more can be briefly explained. Using a similar procedure as the calculations for the ω and 2ω components, we obtain the result that phase reversal occurs as m is only odd. Accordingly, phase reversal on the surface of a specimen can be investigated as long as the phases for $m=1,3,5,7,\ldots$ are observed. However, it is difficult to observe phase reversal for higher order odd components because they are small compared to the ω components in general. Due to this, phase reversal on the surface of the specimen can be investigated to a sufficient extent so long as the ω phase signal is observed.

Here, we briefly describe the features of the 2ω amplitude feedback signal (A_2) used in the NC-SNDM measurement. If A_1 is utilized as the feedback signal, the possibility that the probe tip contacts the surface of the specimen is very high because A_1 is momentarily zero as phase reversal in θ_1 occurs. However, the phase reversal in θ_2 does not occur even though phase reversal in θ_1 occurs, as mentioned above. For this reason, A_2 is usually utilized for the feedback signal to observe the topography of the specimen in the NC-SNDM measurement. By using A_2 as the feedback signal to observe the topography, the A_1 and θ_1 signals can be used to investigate the variation and sign of the slope, respectively, of the $C(V)$ curve on the surface of the specimen, as mentioned above. Thus, if a variation in and the sign of the slope of the $C(V)$ curve can be observed, the microscopic $C(V)$ curve on the surface of the specimen can be guessed from the NC-SNDM measurement. It is thus important to investigate not only the topography with the atomic structure but also A_1 and θ_1 originating from the microscopic properties of the surface of the specimen simultaneously by the NC-SNDM technique.

In a system of a metallic surface such as graphite and a probe tip with a nanogap, corresponding to the situation for STM, the NC-SNDM technique can detect not only the ω amplitude signal, the ω phase signal and topography, but also the current signal originating from the tunneling effect by the applied alternating voltage. In the NC-SNDM measurement, the tunneling current, which is induced between the probe tip and the metallic surface, is modulated by the applied alternating voltage to the specimen and is different from that for STM. Similar to the procedure for the SNDM signal, $I[V(t)]=I[V_A\sin(\omega t)]$ can be expanded by the basis functions $[\sin(m\omega t)$ and $\cos(m\omega t)$, $m=1,2,3,\ldots]$ because the $I(V)$ curve originating from the tunneling effect is generally nonlinear, as shown in Fig. 5(a). This yields

$$I[V(t)] = I_0 + \sum_{m=1}^{\infty} [a_m^c \cos(m\omega t) + b_m^c \sin(m\omega t)], \quad (14)$$

where

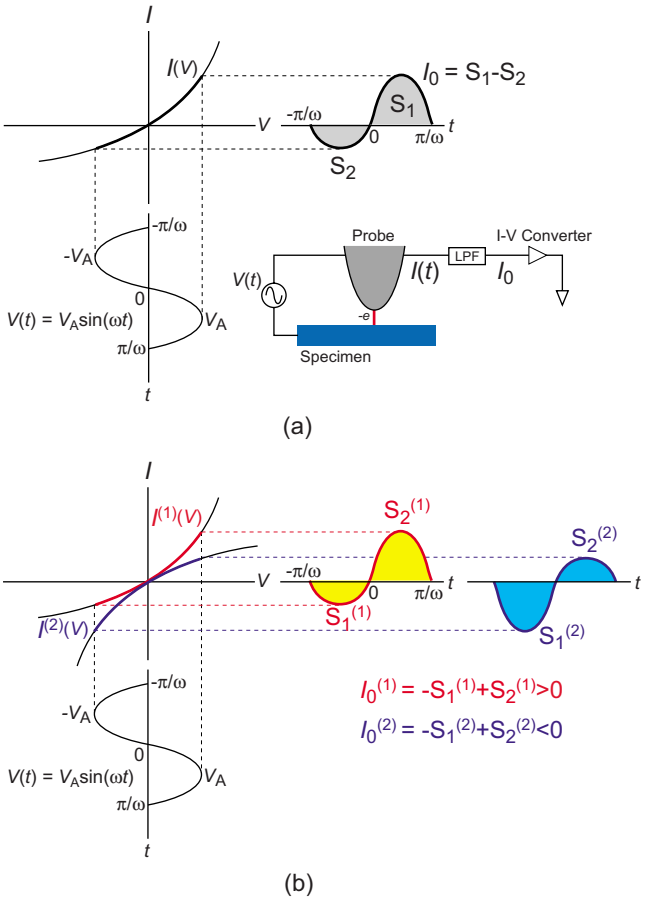

FIG. 5. (Color online) (a) An illustration of the modulated wave of the current by the applied alternating voltage. If the $I(V)$ curve is linear, the modulated wave is a sin wave, and the direct current component (I_0) is 0. However, I_0 is not 0 because the $I(V)$ curve originates from tunneling in the nanojunction between the metallic surface and the metallic probe. (b) The illustration of the modulated waves for the $I^{(1)}(V)$ and $I^{(2)}(V)$ curves. The slope for the $I^{(1)}(V)$ curve increases with increasing V while the slope for the $I^{(2)}(V)$ curve decreases with increasing V. Accordingly, the direct current component $I^{(1)}(V)$ curve is positive while the direct current component $I^{(2)}(V)$ curve is negative.

$$I_0 = \frac{\omega}{2\pi}\int_{-\pi/\omega}^{\pi/\omega} I[V_A \sin(\omega t)]dt, \tag{15}$$

$$a_m^c = \frac{\omega}{\pi}\int_{-\pi/\omega}^{\pi/\omega} I[V_A \sin(\omega t)]\cos(m\omega t)dt, \tag{16}$$

$$b_m^c = \frac{\omega}{\pi}\int_{-\pi/\omega}^{\pi/\omega} I[V_A \sin(\omega t)]\sin(m\omega t)dt. \tag{17}$$

However, I_0, which is a first order and direct current component in the $I[V(t)]$ curve, is only observed in the NC-SNDM measurement because of the low-path filter (<30 kHz) in the oscillator as shown in Fig. 2(a). Here, we consider the effect of the current originating from the microwave (I_m). Since the amplitude of the microwave is generally much smaller than that of the applied alternating voltage ($|V_A|$) in the SNDM measurement, the $I_m(V)$ curve is considered to be linear. For this reason, the direct current component obtained from the $I_m(V)$ curve is considered to be canceled, and the contribution of the microwave is neglected. Hence, we do not need to consider the contribution of the microwave to the current signal. Finally, we consider the two current-voltage curves shown in Fig. 5(b) to understand the characteristics of I_0. The curvature is positive in the case of the red solid line $[I^{(1)}(V)]$. Therefore, $I_0^{(1)} \geq 0$. On the other hand, the curvature is negative in the case of the blue solid line $[I^{(2)}(V)]$. Therefore, $I_0^{(2)} \leq 0$. Thus, by investigating the sign of I_0, we can guess the shape of the $I(V)$ curve within $\pm V_A$ in the NC-SNDM measurements. I_0 is also an important parameter to understand the characteristics of the surfaces of conducting materials.

III. EXPERIMENTAL METHOD

In this study, we used graphite in the form of HOPG and a gold surface, Au(111). HOPG was synthesized by chemical-vapor deposition of polycrystalline graphite with an ordered c-axis orientation. Au(111) structures were fabricated on mica by a general deposition method. The NC-SNDM and STM measurements were carried out with a homebuilt SNDM/STM. Electrochemically etched Pt-Ir probes were used as SNDM and STM tips because it is hard to anneal a probe connected to the oscillator. STM images were obtained at room temperature in an ultrahigh vacuum with a tunneling current (I) of 0.5 nA and a bias voltage (V) of 0.1 V in a constant current mode. NC-SNDM images were also obtained at room temperature in ultrahigh vacuum. The amplitude and frequency of the alternating voltage used in the NC-SNDM measurements were 0.4 $V_{p\text{-}p}$ and 30 kHz, respectively. In order to control the gap between the probe tip and the surface with high sensitivity, the 2ω amplitude signal was used as the feedback signal. Under this noncontact condition, the ω amplitude signal, phase signal, and direct current can be simultaneously detected. The detailed principle of NC-SNDM is described in Sec. II.

IV. EXPERIMENTAL RESULTS AND DISCUSSIONS

A. Graphite surface

Figure 6(a) shows the topographical image of the graphite surface observed using NC-SNDM. To obtain the topological image, the 2ω amplitude signal (A_2) was utilized as the feedback signal. The average of the height in the topographical image is zero. Two patterns were observed in the topographical image excluding the edge part originating from the structure of the HOPG. Here, we will not discuss the origin of the signal at the edge. In order to compare the quality of the upper image with the lower image in the topography, we investigated the error image shown in Fig. 6(b). The error image corresponds to the observed feedback signal. If a perfect feedback system is realized, the signals in the error image are uniform. In this measurement, the A_2 feedback signal was set at 600 Hz which corresponds to the red line in the scale bar. The error image of the upper part is reflected in the topography more distinctly than that of the lower part, as

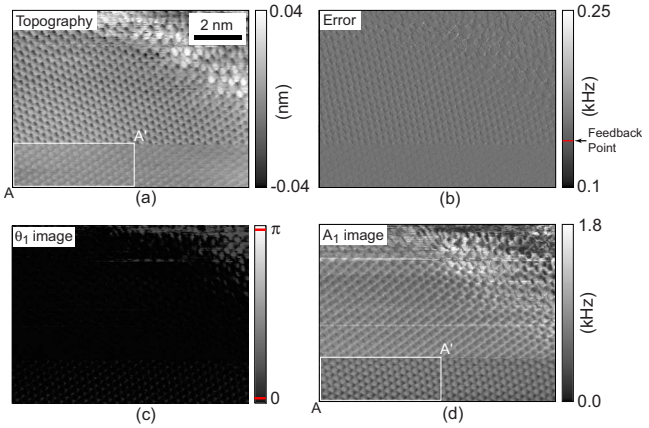

FIG. 6. (Color online) (a) Topographical image of the graphite surface obtained using the NC-SNDM technique. The feedback signal utilizes the 2ω amplitude (A_2) signal. The applied alternating voltage is 0.4 $V_{p\text{-}p}$. (b) Error image corresponding to the observed A_2 signal which is the feedback signal. In this measurement, the A_2 feedback signal was set at 600 Hz. (c) Simultaneous ω phase (θ_1) image of the graphite surface with the topography. (d) Simultaneous A_1 image of the graphite surface with the topography.

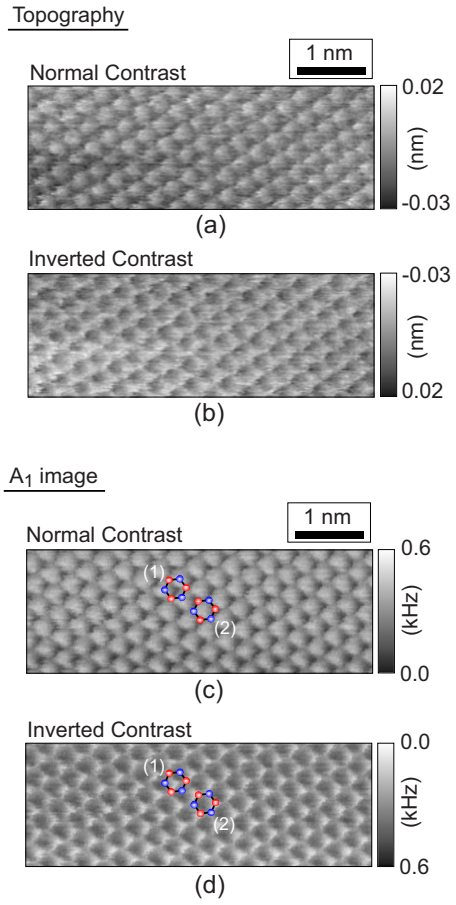

FIG. 7. (Color online) (a) An expanded view topography of the square (A, A′) in Fig. 6(a). The contrast in the figure is the same as that in Fig. 6(a). (b) A_1 image which is an expanded view of the square (A, A′) in Fig. 6(d). Similar to Fig. 7(a), the contrast of the figure is the same as that in Fig. 6(d). (c) Topography which is the same as that of Fig. 6(a). The contrast is changed from normal to inverted contrast. (d) A_1 images, which are the same as that of Fig. 6(b). Similar to Fig. 6(c), the contrast is changed from normal to inverted contrast.

seen in Fig. 6(b). For this reason, the lower image in the topography reflects a better feedback system than the upper image. Similar changes in the pattern in the topography are frequently observed in the STM measurements. Accordingly, the origin of the change in the pattern in the topography by NC-SNDM is considered to be the condition of the probe tip. It is also necessary to consider not only the surface structure but also the condition of the probe tip to understand the origin of the SNDM signal.

The characteristics of the topography observed by NC-SNDM are next described. Here, we only consider the lower part in Fig. 6(a) because of the higher quality of the lower image than that of the upper image. A number of convex spots in the topography by NC-SNDM are observed with a period of ~0.25 nm. This value is consistent with the distance between alternating atomic sites in the signal hexagonal ring or the centers of two neighboring hexagonal rings, as seen in Fig. 1(a). Considering the quality of the topography, we cannot distinguish the periodic structure originating from alternating atomic sites in the signal hexagonal ring from the periodic structure originating from the centers of neighboring rings. To solve this problem, we focus on the simultaneously observed ω amplitude (A_1) image. Fortunately, the quality of the A_1 image is higher than that of the topography originating from the A_2 signal in the graphite surface. Accordingly, we need to investigate the A_1 image in detail to understand the characteristics of the graphite surface observed by NC-SNDM.

Before explaining the A_1 image, we describe the characteristics of the ω phase (θ_1) image. The θ_1 image of the graphite surface is shown in Fig. 6(c). The θ_1 image and the topography in Fig. 1(a) were simultaneously observed in the same area. The θ_1 image was detected under the condition that the A_2 signal was constant for maintaining a constant distance between the probe tip and graphite surface. The value of the phase signal observed by NC-SNDM was not π but ~0 in all areas of the θ_1 image, although the pattern was barely observed. This indicates that the sign of the slope of the $C(V)$ curve in the scanned area is not changed and is negative even though the magnitude of the slope of the $C(V)$ curve is changed. The slope of the $C(V)$ curve observed in this measurement is the same as that for the n-type MIS diode. Thus, phase reversal of the A_1 signal does not occur for the graphite surface.

Figure 6(d) shows the A_1 image of the graphite surface. The A_1 image and the topography in Fig. 6(a) were simultaneously observed in the same area. The A_1 image as well as the θ_1 image were also detected under the condition that the A_2 signal was constant. The quality of the A_1 image for graphite is much higher than that for the topography obtained by the A_2 feedback signal. This indicates that the height dependence of A_1 is remarkable compared to A_2 for the graphite surface. A clear periodic structure and a number of hollow spots, with threefold symmetry, were observed in the A_1 image. To investigate the complicated structure observed in the A_1 image, we expanded the squares drawn in Figs. 6(a) and

6(d). The expanded A_1 image is shown in Fig. 7(c). The expanded topography is also shown in Fig. 7(a) to compare the topography with the A_1 image. The area of the expanded topography is the same as that of the expanded A_1 image. Furthermore, the inverted contrast images of the topography and the A_1 signal are also shown in Figs. 7(b) and 7(d), since Atamny *et al.*[23] pointed out that the inverted contrast image of the graphite by the STM reflects a "true" atomic surface. Next, in the following paragraphs, we describe the characteristics of the SNDM images for the normal and inverted contrast in detail.

Figures 7(a) and 7(c) show the topography and A_1 image for the normal contrast, respectively. Not only a number of convex spots but also hollow spots surrounded by the convex sites were observed, although a large number of convex spots, with threefold symmetry, were only observed in the topography. Investigating the hollow sites, we found that the distance between two hollow sites is consistent with the distance between alternating carbon sites (*A*-*A* or *B*-*B*) in the signal hexagon as shown in Fig. 1(b). However, this distance is the same as the distance between the centers of two hexagonal rings. We can thus consider two arrangements of the single hexagonal ring corresponding to cases (1) and (2) in Fig. 7(c). In case (1), alternating carbon atoms, corresponding to the blue circle in the single hexagonal ring, are positioned on the convex site, and the center of the hexagonal ring is positioned on the hollow site, as shown in Fig. 7(c). In contrast, in case (2), the center of the single hexagonal ring is positioned on the convex site, and alternating carbon atoms corresponding to the red or blue circle are positioned on three hollow sites as shown in Fig. 7(c). The arrangement in the case of (1) is similar to that for the patterns reported in a number of studies on STM measurements. If the origin of the SNDM signal is similar to that of the STM for the graphite surface, there is a possibility that NC-SNDM may detect *A* and *B* sites in the hexagon. However, in the STM study by Atamny *et al.*,[23] the honeycomb structure and the hollow site corresponding to alternating carbons in the single hexagon was observed and the possibility that the hollow site in normal contrast topography by the STM may be the alternating carbon atoms in the single hexagonal ring was pointed out. Hence, we cannot determine the position of the carbon site or hexagon from the topography or the A_1 image for the normal contrast. Similar to the study by Atamny *et al.*,[23] it is necessary to investigate the topography and A_1 image for the inverted contrast in detail in order to determine the position of the carbon sites.

The topography and A_1 image for the inverted contrast are shown in Figs. 7(b) and 7(d). The atomic structure in the graphite surface could not be confirmed in the topography for the inverted or normal contrast. However, a clear honeycomb structure could be recognized in the A_1 image for the inverted contrast. This indicates that the structure made up of graphene could be directly observed by NC-SNDM. The A_1 image for the inverted contrast for the NC-SNDM measurement shows a much clearer and sharper hexagon compared to the similar STM image by Atamny *et al.*[23] Accordingly, we could determine the position of the carbon. In this measurement, the arrangement of the hexagon is considered to correspond to the case of (2). As a result, the hollow and

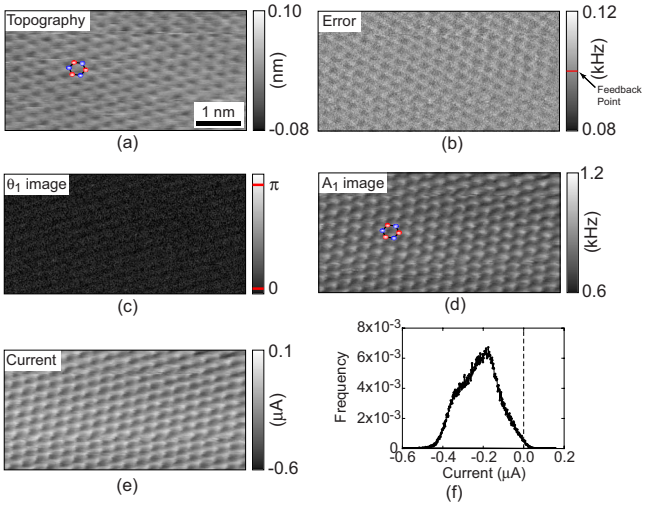

FIG. 8. (Color online) (a) Topographical image of the graphite surface obtained using the NC-SNDM technique. The probe and surface used in Fig. 7 were different from those in Figs. 6 and 7. The applied alternating voltage was 0.4 $V_{p\text{-}p}$. (b) Error image corresponding to the A_2 signal which is a feedback signal. In this measurement, the feedback signal was set at 400 Hz. (c) Simultaneous θ_1 image of the graphite surface with the topography of Fig. 7(a). (d) Simultaneous A_1 image of the graphite surface with the topography of Fig. 7(a). (e) The current image of the graphite surface with the topography of Fig. 7(a). (f) The distribution of the current signal in the scanned area. In this measurement, almost all current signals are negative.

convex sites correspond to every other carbon and the center of the hexagon, respectively. Similar characteristics were observed in the STM images for inverted contrast by Atamny *et al.*[23]

The NC-SNDM technique can detect not only the topography and the SNDM images but also the current image as seen in Fig. 2(a). As indicated in Figs. 8(a)–8(f), we observed not only the error image, the A_1 image, the θ_1 image and topographical image, but we also simultaneously obtained the current image. Similar to the case of Fig. 7, the A_2 signal was utilized as the feedback signal. The feedback signal is 400 Hz in this measurement. This value is smaller than that of Fig. 7 (600 Hz). This means that the position of the probe tip in this case is higher than of the position for Fig. 7. The characteristics of the topography, error image, A_1 image and θ_1 image are next described before the explanation for the current image. The ratio of the error and feedback signals for Fig. 8 is similar to that for Fig. 7. A detailed comparison of the error signals for Figs. 7 and 8 is shown in Fig. 9(a). Focusing on the topography in Fig. 8(a), we could recognize the structure with sixfold or threefold symmetry. Although there is a possibility that this structure observed in the topography may be a honeycomb structure, the origin of this structure cannot be completely determined for the present resolution. On the other hand, a number of clear convex sites, with threefold symmetry, could be recognized in the A_1 image in Fig. 8(d). Two possibilities are considered to explain the origin of the convex sites, with threefold symmetry, in the A_1 image. One is the same case as the A_1 image in Fig. 7(d). In this case, the convex site corresponds to the center of

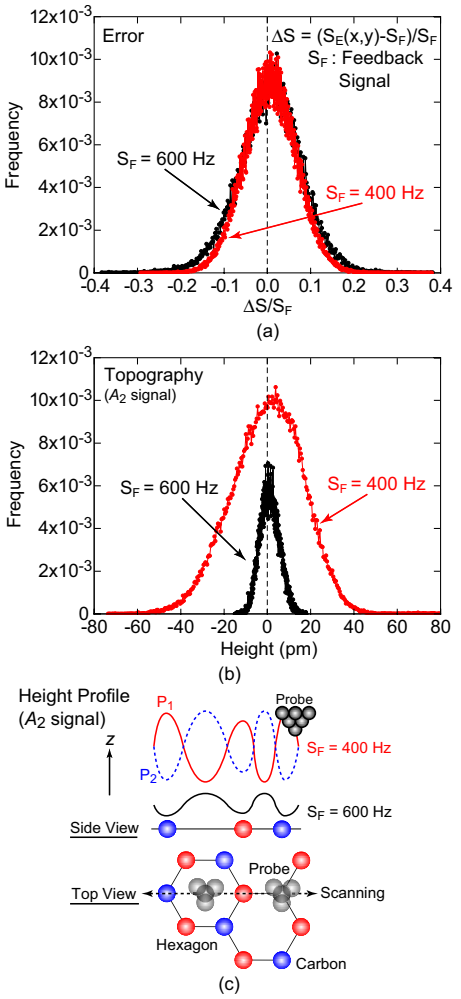

FIG. 9. (Color online) (a) The distributions of the error signal in the scanned area for Figs. 7 and 8. (b) The distributions of the height obtained from the topography by the A_2 feedback signal in the scanned area for Figs. 7 and 8. (c) The illustration of the height profile by the A_2 feedback signal for Figs. 7 and 8.

the hexagon, from consideration of Fig. 7(d). A second possibility is the arrangement of the single hexagon as illustrated in Fig. 8(a). In this case, the convex site corresponds to the position of the carbon. Unfortunately, the honeycomb structure could not be completely recognized in the A_1 image in Fig. 8(d) even though the contrast is inverted similar to the case of Fig. 7(b) and 7(d). Hence, we could not distinguish between the convex site corresponding to the position of alternating carbon atoms and the center of a single hexagon. Thus, measurements with higher resolution are needed to resolve this problem. Finally, we describe the θ_1 image. Phase reversal was not observed in this measurement as well, as shown in Fig. 8(c). The value of the θ_1 signal is the same as that for Fig. 6(c). This suggests that the sign of the slope of the $C(V)$ curve in this measurement is the same as that in Fig. 6(c). Thus, the anomalies originating in the surface structure were not recognized in the θ_1 image for the measurements in Fig. 8 as well as those in Fig. 6.

The crucial point in the measurement for Fig. 8 is that the current image is similar to the A_1 image. Figure 8(e) shows the current image obtained by the A_2 feedback system. The signals in the current image are modulated by the applied alternating voltage. As mentioned in Sec. II, the direct current component originating from the nonlinear $I(V)$ curve is only observed in the NC-SNDM measurement because of the low-path filter, as seen from Fig. 2(a). The current image in Fig. 8(e) is similar not to the A_2 amplitude image but rather to the A_1 amplitude image. This indicates that the variation of the $C(V)$ curve within $\pm V_A$ reflects the direct current component (I_0) originating from the nonlinear $I(V)$ curve by the tunneling effect within $\pm V_A$. The distribution of the current signal in Fig. 8(e) was investigated to understand the characteristics of the current signal in detail. Figure 8(f) shows the distribution of the current signal in Fig. 8(e). The sign of the I_0 signal obtained by NC-SNDM is negative in the scanned area. This indicates that the $I(V)$ curve observed between the probe tip and the graphite is similar to the $I^{(2)}(V)$ curve in Fig. 5(b). This is a very important result to understand the origin of the $C(V)$ curve. The relationship between the $C(V)$ and $I(V)$ curve and the origin of the $C(V)$ curve are discussed in the section on model calculations.

The distributions of the error signals and height signals (A_2) of the topography obtained from the A_2 amplitude feedback signal for Figs. 7 and 8 were also investigated. Figure 9(a) shows the distribution of the error signals in the scanned area for Figs. 7(b) and 8(b). The error signal plotted in Fig. 9(a) ($\Delta S/S_F$) is defined as $\Delta S/S_F=[S_E(x,y)-S_F]/S_F$, where $S_E(x,y)$ and S_F denote the error signals at the (x,y) position in the scanned area and the A_2 feedback signal to observe the topography. As seen from Fig. 9(a), both distributions of the error signal are almost similar and symmetric around $\Delta S/S_F=0$. This means that the relationship between the topography height of the graphite surface and the A_2 feedback signal is linear for both cases. If the A_2 height $[A_2(d)]$ curves for Figs. 7 and 8 are the same, the sensitivity of the height for Fig. 8 is considered to be lower than that for Fig. 7 because the position of the probe tip in Fig. 7(a) ($S_F=600$ Hz) is lower than for Fig. 8(a) ($S_F=400$ Hz). The difference between both distributions of the height of the topography obtained from Figs. 7(a) and 8(a) was clearly recognized. The distribution of the height in Fig. 8(a) is extended to a greater extent than in Fig. 7(a). This means that the variation in the position of the probe tip in Fig. 7(a) is smaller than that in Fig. 8(a). In addition, the honeycomb structure was clearly observed in the measurement not in Fig. 8 but rather in Fig. 7. It is important to consider the reasons for the difference between the two measurements.

The height dependence of the height profile is guessed to understand the situation in Figs. 7(a) and 8(a). The profile of the height in Fig. 7(a) is different from that in Fig. 8(a), as shown in Fig. 9(c). The solid black line corresponds to the height profile guessed from Fig. 7(a) since the A_2 feedback signal is constant. As explained in Fig. 7, the highest position in the height profile corresponds to the center of the hexagon. In contrast, the hollow spot corresponds to the position of the alternating carbons in the hexagon. It is important to understand why the highest position in the height profile corresponds to the center of the hexagon. The key to understand that the hollow spot corresponds to the position of alternating carbon in the hexagon is STM studies by Atamny *et al.*[23]

They suggested that the interaction between the probe tip and the graphite surface is very important in this system because the size of the atom on the surface is similar to that of the probe tip. Accordingly, the atomic number which contributes to the interaction between the probe tip and graphite surface is the maximum as the probe tip is positioned on the center of the hexagonal ring as seen from Fig. 9(c). For this reason, it is considered that the highest position of the probe tip corresponds to the center of the hexagonal ring for the STM by Atamny *et al.* Although the section on calculations and discussions is described, NC-SNDM as well as STM can detect the tunneling effect. Consequently, we can understand that the highest position of the probe tip is the center of the hexagon in the case of the NC-SNDM measurement. Thus, not only in the STM but also in the NC-SNDM measurement, the interaction between the probe tip and graphite surface is very important. Therefore, the profile of the height, which is guessed as shown in Fig. 9(c), is considered to be reasonable.

On the other hand, the profile of the height guessed from Fig. 8(a) is considered to be two simple cases due to the poor resolution, and is illustrated by the red solid (P_1) line and the blue dotted (P_2) line in Fig. 9(c). The former is the lowest at the center of the hexagon while the latter is the highest at the center of the hexagon. To guess which height profile of P_1 or P_2 was realized in Fig. 8, we assume a spatial change from the case of Fig. 7 to that of Fig. 8. Retracting from the probe tip from the case of Fig. 7 to the case of Fig. 8, the height profile is considered to be changed from the black solid line corresponding to Fig. 7(a) to the red solid line in the case of P_1 which corresponds to Fig. 8(a). This means that the interaction between the probe tip and the graphite surface is changed by changing the height of the feedback. Therefore, the height profile for Fig. 8(a) can be guessed to correspond to the case of P_1. Thus, the periodic and complicated structure observed in the topography in Fig. 8(a) can be assumed to reflect the honeycomb structure differently from the case of Fig. 7 due to the height profile for P_1. As a result, a number of convex sites with threefold symmetry in Fig. 8(d) can also be guessed to be carbon sites. Thus, we can obtain the origin of the pattern of the SNDM images in Fig. 8 from the relationship of the height profile between Figs. 7 and 8. However, it is difficult to further discuss the characteristics of images in Fig. 8 so long as the SNDM images with higher resolution than those in Fig. 8 can be observed.

B. Au(111) Surface

The well-known Au(111) surface was also observed by NC-SNDM and STM. Thus, not only the graphite surface but also the Au(111) surface could be observed by NC-SNDM to investigate whether the SNDM image can be observed on another metallic surface. Prior to the NC-SNDM measurement, we confirmed the surface of the Au(111) by STM. Figure 10(a) shows an STM image of the Au(111) surface. Although the resolution is poor, the periodic structure originating from the ordered surface of Au(111) could be observed. Since the Au(111) surface could be confirmed by STM, we carried out the NC-SNDM measurement on the same area. Unfortunately, a periodic structure in the topography similar to that in the STM image was not observed in the NC-SNDM measurement. For this reason, we tried to observe the approach curve as well as the SNDM images in order to easily confirm whether the SNDM images of the metallic surface were finite. The approach curve of θ_1 and θ_2 for the Au(111) surface are shown in the upper figure in Fig. 10(b). The approach curve of A_1 and the current signals for the Au(111) surface are shown in the lower figure in Fig. 10(b). As the probe tip approached the Au(111) surface, the values of θ_1 and θ_2 became $\theta_1 \sim -10°$ and $\theta_2 \sim -160°$, respectively. This indicates that the Au(111) surface as well as the graphite surface has a nonlinear $C(V)$ curve. The values for θ_1 and θ_2 of Au(111) are the same as those for graphite. A_1 tends to be enhanced by the probe tip approaching the Au(111) surface. Thus, we could also confirm the SNDM signal for the Au(111) surface by using the approach curve measurement. Furthermore, the approach curve of the current signal could also be observed, and the sign of the current signal is basically negative near the Au(111) surface although the current at the position of the probe tip near the surface is positive. The sign of the current for Au(111) is considered to be the same as that for the graphite. Thus, there is a possibility that the characteristic of the graphite surface may be similar to that of the Au(111) surface. This result is useful to understand the origin of the mesoscopic capacitance between the metallic surface and probe.

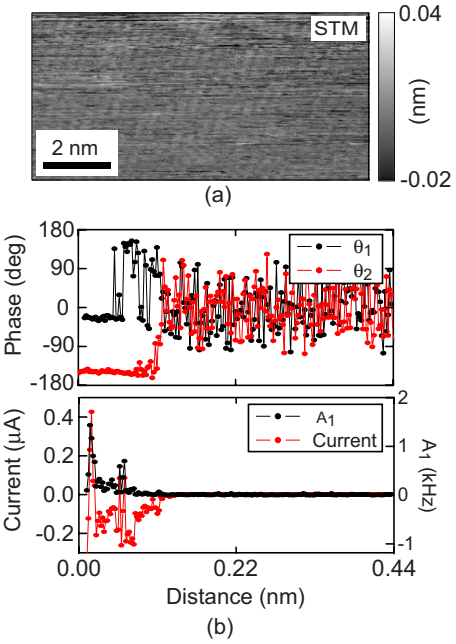

FIG. 10. (Color online) (a) Topographical image of the Au(111) surface obtained by STM. (b) The upper figure is the approach curve of the θ_1 and θ_2 signals. The lower figure is the approach curve of the A_1 and current signals.

C. Model calculations

1. Electrochemical capacitance in a nanojunction

One should consider the origin of the $C(V)$ curve in a system with tunneling between two metallic electrodes in

order to understand the origin of the SNDM images for the graphite surface. The key to understanding the origin of the $C(V)$ curve is the STM study by Hou *et al.*[26] They experimentally demonstrated the importance of the *electrochemical* capacitance originating from the local density of states for the probe tip and self-assembled monolayers by using STM. On the other hand, theoretical studies of the electrochemical capacitance in the system with and without tunneling between two metallic electrodes are being advanced not only due to STM studies but also due to recent developments of various nanodevices.[27–34] Theoretical studies suggest that the electrochemical capacitance in a nanojunction is composed of the classical capacitance of the gap between the two electrodes, the electrochemical capacitance originating from the local density of states at the surface of the electrode and the contribution of the tunneling. Accordingly, by substituting the probe tip and the graphite surface for both electrodes, we can easily understand that the capacitance observed by NC-SNDM originates in the gap between the probe tip and the graphite surface. This indicates that there is a possibility that the origin of the $C(V)$ curve observed in the NC-SNDM measurement may be reflected in the local density of states in the surface structure of the graphite.

To interpret the SNDM images for a graphite surface, we focused on the theoretical studies of the electrochemical capacitance with a leaky nanocapacitor by Zhao *et al.*[33] An electrochemical capacitance with a leaky nanocapacitor originated from the tunneling effect has three regions, two scattering regions and two electrodes which correspond to the probe tip and metallic surface as shown in Fig. 11(a). Here, the two scattering regions correspond to regions (Ω_s and Ω_t) of scattering and the transition of electrons between two metallic electrodes as shown in Fig. 11(a). The electrochemical capacitance is closely related to the variation of the local band, $-eU_t$ and $-eU_s$, in Ω_t and Ω_s. U_t and U_s are induced by the internal potential originating from Coulomb interaction as V_t and V_s are applied to the metallic surface and probe, respectively[33] as seen from Fig. 11(b). It is to be noted that U_t and U_s are different from the applied voltages $-eV_t$ and $-eV_s$, which occur at contacts far away from the variation in the barrier.

a. First-order electrochemical capacitance, C_{11} . We now estimate the first-order electrochemical capacitance between the probe tip and the graphite surface, C_{11}. At equilibrium conditions, the electron energies for the probe tip (s) and metallic surface (t) near the barrier are given by $E_{tt}(V_s,V_t)=E_F-eV_t-eU_t(V_s,V_t)$, $E_{ts}(V_s,V_t)=E_F-eV_t-eU_s(V_s,V_t)$, $E_{st}(V_s,V_t)=E_F-eV_s-eU_t(V_s,V_t)$ and $E_{ss}(V_s,V_t)=E_F-eV_s-eU_s(V_s,V_t)$, respectively. Here, E_F is the Fermi energy for the probe tip and metallic surface without an applied voltage, and E_{tt} and E_{ss} denote the energies corresponding to the electron incidented from the probe tip and metallic surface, which are scattered back to the probe and metallic specimen. E_{ts} and E_{st} denote electron energies which are launched at the probe tip and metallic surface but end up in the probe and metallic specimen. Next, we present the number of electrons in the metallic surface (s) and probe tip (t) incident from the contact s,t by $\sigma_{\alpha\beta}$ ($\alpha,\beta=s,t$). The number of electrons incident from the metallic specimen to the metallic surface is

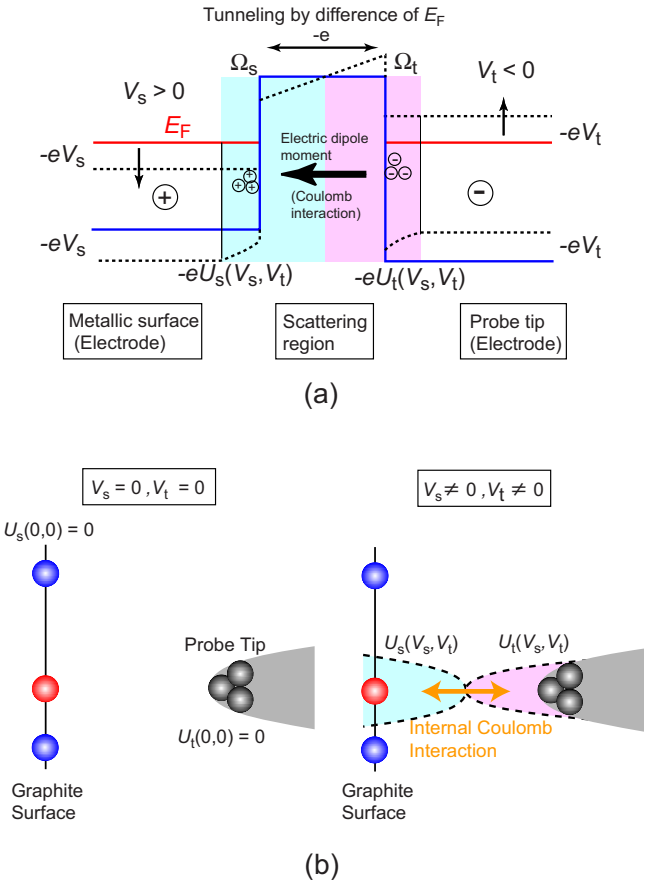

FIG. 11. (Color online) (a) Relationship between the metallic surface and probe for $V_s=0$ and $V_t=0$, where V_s and V_t are the voltages applied to the metallic surface and the probe, respectively. (b) Relationship between the metallic surface and probe for $V_s\neq 0$ and $V_t\neq 0$. In this case, the gap between the metallic surface and probe tip is divided into two regions of Ω_s and Ω_t, and surface potentials, $U_s(V_s,V_t)$ and $U_t(V_s,V_t)$ are induced by the applied voltage and internal coulomb interaction between the metallic surface and probe tip.

expressed as $\sigma_{ss}=\sigma_{ss}(E_{ss})=\sigma_{ss}[E_F-eV_s-eU_s(V_t,V_s)]$. The number of electrons incident from the probe to the probe tip is expressed as $\sigma_{tt}=\sigma_{tt}(E_{tt})=\sigma_{tt}[E_F-eV_t-eU_t(V_t,V_s)]$. The number of electrons incident from the probe tip to the metallic surface is expressed as $\sigma_{st}=\sigma_{st}(E_{st})=\sigma_{st}[E_F-eV_t-eU_s(V_t,V_s)]$. The number of electrons incident from the metallic surface to the probe tip is expressed as $\sigma_{ts}=\sigma_{ts}(E_{ts})=\sigma_{ts}[E_F-eV_s-eU_t(V_t,V_s)]$. As shown in Fig. 12, the charges measured from the equilibrium value in the probe tip and metallic surface are expressed as $\Delta Q_t(V_s,V_t)=\Sigma_{\alpha=s,t}\Delta N_{t\alpha}(V_s,V_t)=\Sigma_{\alpha=s,t}\{\sigma_{t\alpha}[E_{t\alpha}(V_s,V_t)]-\sigma_{t\alpha}(E_F)\}$ and

$$\Delta Q_s(V_s,V_t)=\Sigma_{\alpha=s,t}\Delta N_{s\alpha}(V_s,V_t)$$
$$=\Sigma_{\alpha=s,t}\{\sigma_{s\alpha}[E_{s\alpha}(V_s,V_t)]-\sigma_{s\alpha}(E_F)\}$$

respectively. Accordingly, we can obtain

$$\Delta Q_t(V_s,V_t)=C_0(U_t-U_s)=\sum_{\alpha=s,t}\Delta N_{t\alpha}(V_s,V_t), \quad (18)$$

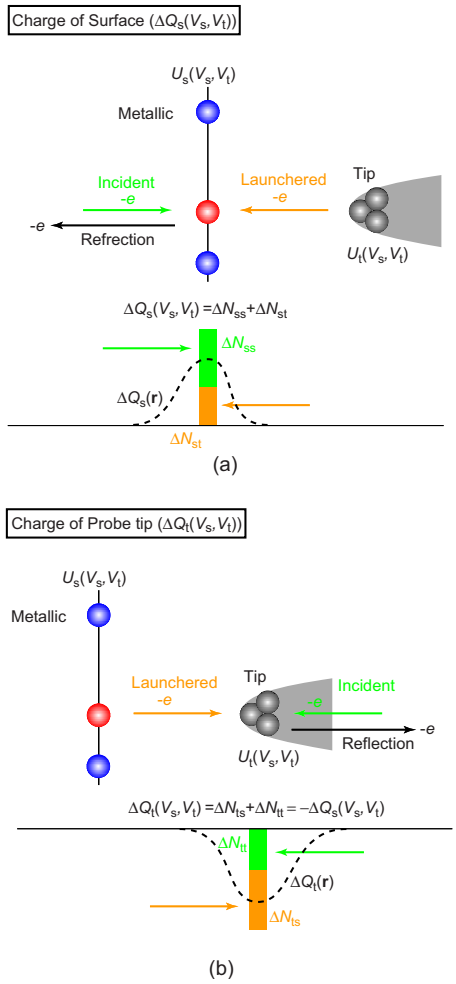

FIG. 12. (Color online) (a) The charge of the metallic surface $[\Delta Q_s(V_s,V_t)]$ upon application of a voltage to the metallic surface and probe. $\Delta Q_s(V_s,V_t)$ is the total of $\Delta N_{ss}+\Delta N_{st}$, where N_{ss} is the number of electrons accumulated from the inside of the metallic material to the surface and N_{st} is the number of electrons emitted from the probe tip to the metallic surface and accumulated on the surface. The dotted line in the distribution of the charge at the metallic surface corresponds to $\Delta Q_s(\boldsymbol{r})$ which is the distribution of the charge expected from the rigorous model. (b) The charge of the probe tip $[\Delta Q_t(V_s,V_t)]$ upon application of a voltage to the metallic surface and probe. $\Delta Q_t(V_s,V_t)$ is the total of $\Delta N_{ts}+\Delta N_{tt}$, where N_{tt} is the number of electrons accumulated from the inside of the probe to the probe tip and N_{ts} is the number of electrons emitted from the metallic surface to the probe tip and accumulated at the probe tip. The dotted line in the distribution of the charge at the probe tip corresponds to $\Delta Q_t(\boldsymbol{r})$ which is the distribution of the charge expected from the rigorous model.

$$\Delta Q_s(V_s,V_t)=C_0(U_s-U_t)=\sum_{\alpha=s,t}\Delta N_{s\alpha}(V_s,V_t)=-\Delta Q_t(V_s,V_t). \tag{19}$$

Because the same charge defines the electrochemical capacitance C_μ, given by $C_\mu=e\Delta Q_k/(V_t-V_s)$, we have

$$C_0(U_t-U_s)=C_\mu(V_t-V_s). \tag{20}$$

Expanding Eqs. (18) and (19) with respect to V_t-U_t, V_s-U_t, and V_s-U_t, V_s-U_s, we can expand $C_0(U_t-U_s)=C_0[U_t(V_t,V_s)-U_s(V_t,V_s)]$ and obtain

$$C_0(U_t-U_s)=\sum_{n=1}^{\infty}\frac{1}{n!}\frac{d^{(n)}\sigma_{tt}(E_{tt})}{dE_{tt}^{(n)}}(V_t-U_t)^n+\sum_{n=1}^{\infty}\frac{1}{n!}\frac{d^{(n)}\sigma_{ts}(E_{ts})}{dE_{ts}^{(n)}}(V_s-U_t)^n, \tag{21}$$

$$C_0(U_s-U_t)=\sum_{n=1}^{\infty}\frac{1}{n!}\frac{d^{(n)}\sigma_{st}(E_{st})}{dE_{st}^{(n)}}(V_t-U_s)^n+\sum_{n=1}^{\infty}\frac{1}{n!}\frac{d^{(n)}\sigma_{ss}(E_{ss})}{dE_{ss}^{(n)}}(V_s-U_s)^n. \tag{22}$$

Considering the first order only, we get

$$C_0(U_t^{(1)}-U_s^{(1)})\simeq D_{tt}V_t+D_{ts}V_s-(D_{tt}+D_{ts})U_t^{(1)}, \tag{23}$$

$$C_0(U_s^{(1)}-U_t^{(1)})\simeq D_{st}V_t+D_{ss}V_s-(D_{st}+D_{ss})U_s^{(1)}, \tag{24}$$

where $D_{tt}\equiv d\sigma_{tt}(E_F)/dE$, $D_{ts}\equiv d\sigma_{ts}(E_F)/dE$, $D_{st}\equiv d\sigma_{st}(E_F)/dE$, and $D_{ss}\equiv d\sigma_{ss}(E_F)/dE$, respectively. The above partition of the local charge according to where it originates can be equally applied to the scattering from local partial density of states (LPDOS). Hence, for example, D_{ts} is the LPDOS, which is the DOS for an electron incident from the metallic surface passing through the scattering region Ω_t and reaching the probe tip. Similarly, D_{tt} is the LPDOS, which is the DOS for an electron incident from the probe tip passing through the scattering region Ω_t and eventually returning to the probe.[33,35] Both of these LPDOS describe the tunneling process. This latter term is neglected for semiclassical calculations and is nonzero for quantum analysis.[33]

From Eqs. (23), (24), and (20), solving for U_t and U_s, we can obtain

$$U_t^{(1)}=U_t^{(1)}(V_t,V_s)=\frac{(D_{st}V_t+D_{ss}V_s)(C_0+D_{tt}+D_{ts})}{C_0(D_{tt}+D_{ts}+D_{st}+D_{ss})}, \tag{25}$$

$$U_s^{(1)}=U_s^{(1)}(V_t,V_s)=\frac{(D_{tt}V_t+D_{ts}V_s)(C_0+D_{st}+D_{ss})}{C_0(D_{tt}+D_{ts}+D_{st}+D_{ss})}, \tag{26}$$

where $U_t^{(1)}$ and $U_s^{(1)}$ are first-order U_t and U_s. Therefore, the linear electrochemical capacitance of C_μ, C_{11} can be expressed as

$$C_{11} = \frac{C_0(U_t^{(1)} - U_s^{(1)})}{V_t - V_s} = \frac{\left(\frac{D_{tt}}{D_{tt}+D_{ts}} - \frac{D_{st}}{D_{st}+D_{ss}}\right)V_t + \left(\frac{D_{st}}{D_{tt}+D_{ts}} - \frac{D_{ss}}{D_{st}+D_{ss}}\right)V_s}{(V_t - V_s)\left(\frac{1}{C_0} + \frac{1}{D_{tt}+D_{ts}} + \frac{1}{D_{st}+D_{ss}}\right)}. \quad (27)$$

In the semiclassical limit,[33] the LPDOS is given by

$$\frac{d\sigma_{k\alpha}(E_F)}{dE} = D_{k\alpha}(E_F) = \sum_{\beta=t,s} D_k(E_F)\left[\frac{T}{2} + \delta_{\beta\alpha}\left(R\delta_{\beta k} - \frac{T}{2}\right)\right], \quad (28)$$

where T and R are the electron transmission and reflection probabilities of the nanojunction, respectively, $D_t = D_{tt} + D_{ts}$ and $D_s = D_{st} + D_{ss}$ are the total local DOS at the probe tip and the metallic surface. Substituting Eq. (27) into Eq. (28), we finally obtain

$$\frac{R}{C_{11}} = \frac{1}{C_0} + \frac{1}{D_t(E_F)} + \frac{1}{D_s(E_F)}. \quad (29)$$

Note that both C_0 and R are a function of d, which is the gap between the probe tip and the metallic surface. For this reason, $C_{11} = C_{11}(d)$ and C_{11} is independent of V_t and V_s or $V_t - V_s$.

b. Second-order electrochemical capacitance, C_{111} . Furthermore, we can expand Eqs. (18) and (19) to obtain the second-order electrochemical capacitance, C_{111}.

$$C_0(U_t^{(2)} - U_s^{(2)}) \simeq D_{tt}V_t + D_{ts}V_s - (D_{tt} + D_{ts})U_t + \frac{1}{2}\left[\frac{dD_{tt}}{dE_1}(U_t - V_t)^2 + \frac{dD_{ts}}{dE_2}(U_t - V_s)^2\right], \quad (30)$$

$$C_0(U_s^{(2)} - U_t^{(2)}) \simeq D_{st}V_t + D_{ss}V_s - (D_{st} + D_{ss})U_s + \frac{1}{2}\left[\frac{dD_{st}}{dE_3}(U_s - V_t)^2 + \frac{dD_{ss}}{dE_4}(U_s - V_s)^2\right]. \quad (31)$$

Using Eq. (28) and the expression[33]

$$\frac{d^2\sigma_{k\alpha}}{dE^2} = \frac{dD_{k\alpha}}{dE} = \bar{D}_{k\alpha} = \frac{dD_k}{dE}[T + (1-2T)\delta_{\alpha k}] = \bar{D}_k[T + (1-2T)\delta_{\alpha k}] \quad (32)$$

we can obtain

$$C_0(U_t^{(2)} - U_s^{(2)}) \simeq D_t\left(\frac{T}{2} + R\right)V_t + D_t\frac{T}{2}V_s - D_tU_t^{(2)} + \frac{1}{2}\left[\frac{dD_t}{dE_1}R(U_t^{(2)} - V_t)^2 + \frac{dD_t}{dE_2}T(U_t^{(2)} - V_s)^2\right], \quad (33)$$

$$C_0(U_s^{(2)} - U_t^{(2)}) \simeq D_s\frac{T}{2}V_t + D_t\left(\frac{T}{2} + R\right)V_s - D_tU_s^{(2)} + \frac{1}{2}\left[\frac{dD_s}{dE_3}T(U_s^{(2)} - V_t)^2 + \frac{dD_t}{dE_4}R(U_s^{(2)} - V_s)^2\right]. \quad (34)$$

Here, $U_t^{(2)}$ and $U_s^{(2)}$ are the second-order components for U_t and U_s. Since $(U_t^{(2)} - V_t)^2$, $(U_t^{(2)} - V_s)^2$, $(U_s^{(2)} - V_t)^2$, and $(U_s^{(2)} - V_s)^2$ are included in the components which are greater than the second order, we substitute $U_t^{(2)}$ and $U_s^{(2)}$ for $U_t^{(1)}$ and $U_s^{(1)}$, and solve for $U_t^{(2)}$ and $U_s^{(2)}$

$$U_t^{(2)} = U_t^{(2)}(V_t, V_s) = \frac{C_0\beta + (C_0 + D_s)\alpha}{C_0(D_t + D_s) + D_tD_s} \quad (35)$$

$$U_s^{(2)} = U_s^{(2)}(V_t, V_s) = \frac{C_0\alpha + (C_0 + D_t)\beta}{C_0(D_t + D_s) + D_tD_s}. \quad (36)$$

where

$$\alpha \equiv D_t\left(\frac{T}{2} + R\right)V_t + D_t\frac{T}{2}V_s + \frac{1}{2}R\bar{D}_t\left(\frac{T}{2} + \frac{C_{11}}{D_t}\right)^2(V_t - V_s)^2 + \frac{1}{2}RD_t\left(R + \frac{T}{2} - \frac{C_{11}}{D_t}\right)^2(V_t - V_s)^2, \quad (37)$$

$$\beta \equiv D_s\frac{T}{2}V_t + D_s\left(\frac{T}{2} + R\right)V_s + \frac{1}{2}R\bar{D}_s\left(R + \frac{T}{2} - \frac{C_{11}}{D_s}\right)^2 \times (V_t - V_s)^2 + \frac{1}{2}RD_s\left(\frac{T}{2} + \frac{C_{11}}{D_s}\right)^2(V_t - V_s)^2. \quad (38)$$

Similar to the calculation of C_{11}, we calculate $C_0(U_t - U_s)$, yielding

$$C_0(U_t - U_s) = C_{11}(V_t - V_s) + \frac{1}{2}C_{111}(V_t - V_s)^2, \quad (39)$$

where

$$C_{111} = C_{11}\left\{\frac{\bar{D}_s(E_F)}{D_s(E_F)}\left[\frac{T}{2} + \frac{C_{11}}{D_s(E_F)}\right]^2 - \frac{\bar{D}_t(E_F)}{D_t(E_F)}\left[\frac{T}{2} + \frac{C_{11}}{D_t(E_F)}\right]^2\right\} + \frac{T}{R}C_{11}\left\{\frac{\bar{D}_s(E_F)}{D_s(E_F)}\left[R + \frac{T}{2} - \frac{C_{11}}{D_s(E_F)}\right]^2 - \frac{\bar{D}_t(E_F)}{D_t(E_F)}\left[R + \frac{T}{2} - \frac{C_{11}}{D_t(E_F)}\right]^2\right\}. \quad (40)$$

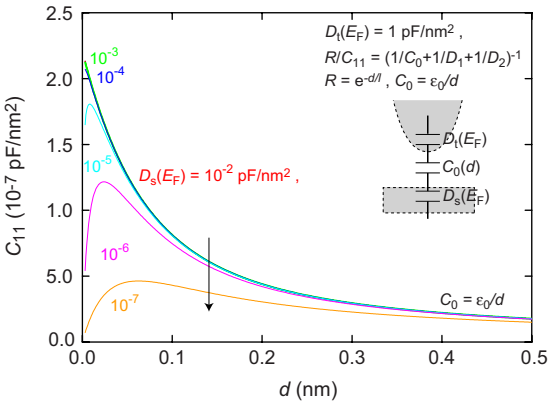

FIG. 13. (Color online) Calculated first-order electrochemical capacitance, C_{11}-d curve $[C_{11}(d)]$. C_{11} is the capacitance for the parallel plate capacitor of $D_t(E_F)$, $D_s(E_F)$, and $C_0(d)$, where $D_t(E_F)$, $D_s(E_F)$, and $C_0(d)$ are the local density of states for the probe tip, the local density of states for the metallic surface, and the classical parallel plate capacitor $[C_0(d)=\epsilon_0/d]$, respectively. R is the reflection probability and expressed as $R=e^{-d/l}$ for the semiclassical model.

As seen from Eq. (39), C_{111} is the second order nonlinear electrochemical capacitance in terms of microscopic quantities such as various LPDOS. Similar to C_{11}, C_{111} depends on d due to $T(d)$, $R(d)$, and $C_{11}(d)$. As $D_t=D_s$ and $\bar{D}_t=\bar{D}_s$, Eq. (40) gives $C_{111}=0$. As a capacitor without dc coupling between the probe tip and metallic surface, i.e., for cases $T=0$, Eq. (40) becomes

$$C_{111}^{\text{class}} = (C_{11}^{\text{class}})^3 \left\{ \frac{\bar{D}_s(E_F)}{[D_s(E_F)]^3} - \frac{\bar{D}_t(E_F)}{[D_t(E_F)]^3} \right\}, \qquad (41)$$

where C_{11}^{class} is the classical electrical capacitance, and corresponds to C_{11} for $R=1$.

If the probe tip is assumed to be approximately comprised of an isolated single atom or a few atoms, it is considered that D_t is larger than D_s, and D_t can be neglected in Eq. (29). For this reason, we choose $D_t=1$ pF/nm². R can be approximately written as $R=1-e^{-d/l}$ where $l\sim(8m\phi/\hbar^2)^{1/2}\sim 0.04$ nm because ϕ and V_A are estimated to be ~ 5 and 0.4 V for the graphite surface.[36–40] However, an understanding of the electrical properties between the probe tip and a metallic surface is needed to establish a strict model and to carry out a strict calculation. In this paper, we neglect the effect of the probe tip in the below discussion in order to understand the capacitance between the probe tip and the metallic surface.

As seen from Fig. 13, $C_{11}(d)$ is smaller than the classical parallel plate capacitance $C_0=\epsilon_0/d$. This can be easily understood from Eq. (29). As tunneling occurs, the $C_{11}(d)$ curve is suppressed by D_s. Considering that $C_{11}(d)$ is used in the NC-SNDM measurement, we cannot expect to obtain an atomic image by using $C_{11}(d)$ due to the smaller variation in the $C_{11}(d)$ curve than the STM or AFM approach curves. In addition, since $C_{11}(d)$ is related to $C_g(d)$ which corresponds to the classical capacitance between the probe and a flat metallic surface because $C_0(d)$ related to $C_g(d)$ is included in $C_{11}(d)$, the contribution of $C_{11}(d)$ is small in $C_g(d)$. Actually, we estimate the $C_g(d)$ curve to investigate the contribution of $C_{11}(d)$ in $C_g(d)$. First, we calculate the $C_g(d)$ curve. Assuming the radius of the probe tip to be 10 nm, the $C_g(d)$ curve is shown in Fig. 14(a). Here,

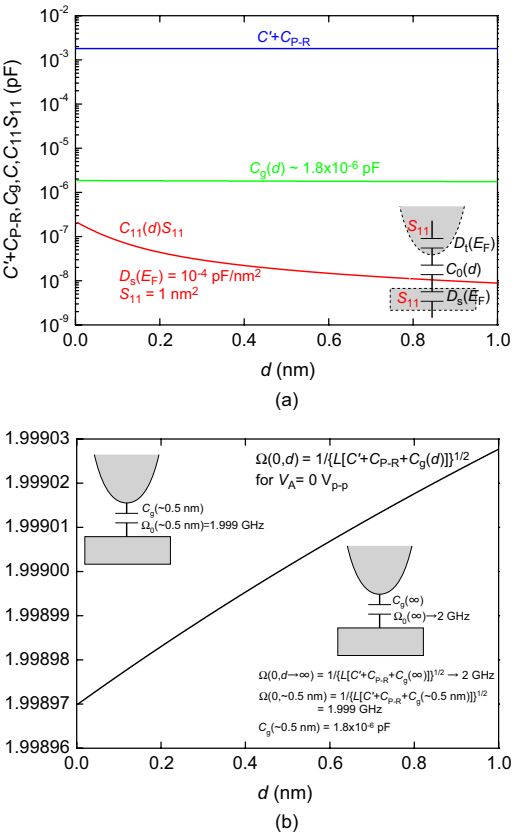

FIG. 14. (Color online) (a) Calculated $C_{11}S_{11}$-d $[S_{11}C_{11}(d)]$ curve for $D_s(E_F)=10^{-4}$ pF/nm² ($C_{11}S_{11}$) and C_g-d $[C_g(d)]$ curves and $C'+C_{P\text{-}R}$. Here, S_{11} is the square area for the capacitor in drawn in the figure and 1 nm². $C_g(d)$ is the classical capacitance between the probe and flat metallic surface. C' is the stray capacitance in the oscillation circuit. $C_{P\text{-}R}$ is the capacitance between the probe and the return ring as shown in Fig. 2. Note that $C+C_{P\text{-}R}$ is not a function of d.

$$C_g(d) = 4\pi\epsilon_0 a\left[1+\frac{a}{r-a}+\left(\frac{a}{r-a}\right)^2+\left(\frac{a}{r-a}\right)^3+2\left(\frac{a}{r-a}\right)^4 + 3\left(\frac{a}{r-a}\right)^5+\cdots\right] \qquad (42)$$

is obtained from the calculation of the capacitance between the metallic sphere and surface where a is the radius of the tip. To compare $C_{11}(d)$ with $C_g(d)$, we need to introduce the effective square area S_{11} and assume that S_{11} is less than 10 nm², at least because the shape of the probe tip is approximately a sphere. In Fig. 14(a), the $C_{11}(d)$ curve for $S_{11}=1$ nm² is also plotted. $C_{11}(d)$ is smaller than $C_g(d)$ for $S_{11}=1$ nm² while $C_{11}(d)$ is comparable to $C_g(d)$ for $S_{11}=10$ nm². Accordingly, it is considered that $C_{11}(d)$ is com-

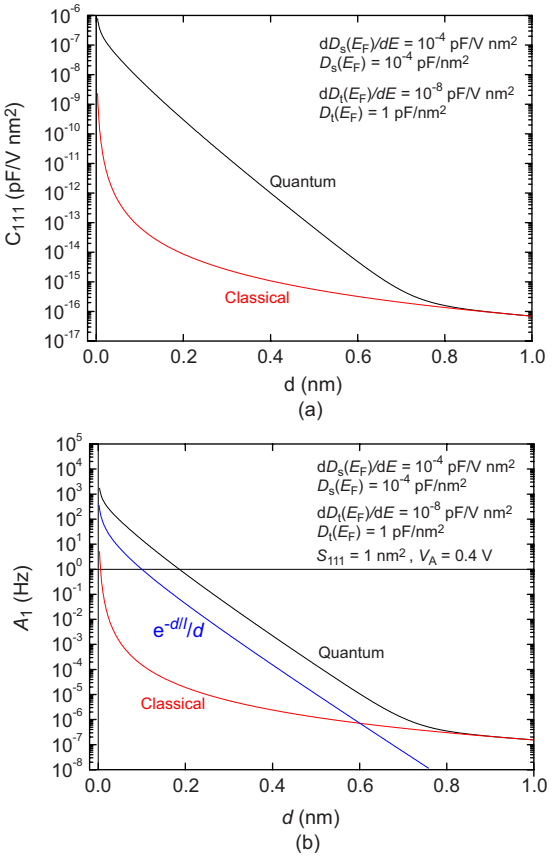

FIG. 15. (Color online) (a) The second-order electrochemical capacitance between the probe tip and the metallic surface $[C_{111}(d)]$ and classical second-order electrochemical capacitance $[C_{111}^{\text{class}}(d)]$ curves. (b) The first-order amplitude signal $[A_1(d)]$ curves. A_1 with the quantum effect can be obtained from the $C_{111}(d)$ curve while A_1 for the classic case without the quantum effect can be obtained from the $C_{111}^{\text{class}}(d)$ curve.

parable to or less than $C_g(d)$, at least in this range. As a result, the contribution of $C_{11}(d)$ is considered to be small in $C_g(d)$. These capacitances are related to the resonance frequency; we cannot expect that $C_{11}(d)$ or $C_g(d)$ correspond to the signal to detect the atomic surface as seen in Fig. 14(a).

We investigated two resonance frequencies without an applied voltage to estimate $C'+C_{\text{P-R}}$ and L. It is very important to investigate $C'+C_{\text{P-R}}$ and L because these values in this system are needed to understand the electrochemical capacitance between the probe tip and metallic surface. One is the resonance frequency $\Omega(0,\sim 0.5\ \text{nm})=\{L[C'+C_{\text{P-R}}+C_g(\sim 0.5\ \text{nm})]\}^{-1/2}$, where $d\sim 0.5$ nm is estimated to be the gap as the probe tip is approached. Another is the frequency $\Omega(0,d\to\infty)=\{L[C'+C_{\text{P-R}}+C_g(d\to\infty)]\}^{-1/2}\to(C'+C_{\text{P-R}})^{-1/2}$ for the large distance between the probe tip and the metallic surface $(d\to\infty)$ due to $C_g(d\to\infty)\to 0$. $\Omega(0,d\to\infty)\sim 2$ GHz and $\Omega(0,\sim 0.5\ \text{nm})\sim 1.999$ GHz are actually obtained from the observation of resonance frequencies at $d\to\infty$ and $d\sim 0.5$ nm. Solving $C'+C_{\text{P-R}}$ and L from $\Omega(0,d\to\infty)$ and $\Omega(0,\sim 0.5\ \text{nm})$, we obtain $C'+C_{\text{P-R}}\sim 1.1\times 10^{-3}$ pF and $L\sim 35\ \mu$H. The $\Omega(0,d)$ curve estimated from the obtained $C'+C_{\text{P-R}}$ and L is shown in Fig. 14(b). We also cannot utilize C_{11} or C_g to detect the atomic surface in the NC-SNDM measurement because $C_{11}(d)S_{11}$ and C_g are much smaller than $C'+C_{\text{P-R}}$, as seen from Fig. 14(b). This indicates that $\Omega(0,d)$ is not applied to the feedback signal to detect the atomic surface due to the poor variation in $\Omega(0,d)$. To resolve this problem, the nonlinear electrochemical capacitance, which is related to the applied voltage, needs to be introduced.

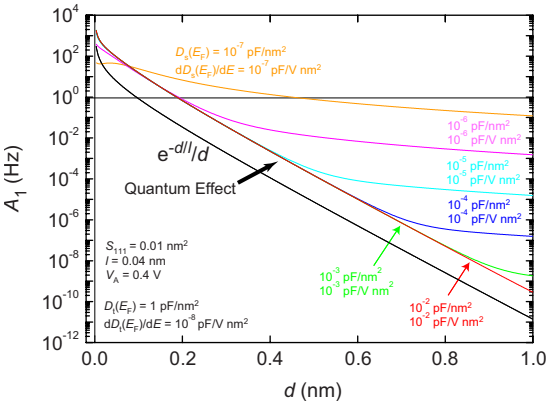

FIG. 16. (Color online) $A_1(d)$ curves with the quantum effect for various $D_s(E_F)$ and $\bar{D}_s(E_F)$. The black solid line is the $e^{-d/l}/l$ curve.

2. SNDM Signal in NC-SNDM

Before calculating the second order electrochemical capacitance $[C_{111}(d)V]$, we need to estimate $\bar{D}_t$ to obtain the $C_{111}(d)$ curve. Scanning tunneling spectroscopy (STS) is a useful reference to estimate $\bar{D}_t$ for the graphite surface. STS on A and B sites in the graphite by STM were strictly simulated by Tsukada *et al.*[41] STS is generally obtained from the $(dI/dV)/(I/V)-V$ curve. To easily understand STS of the graphite surface, we substitute the formula of the tunneling current for a small applied voltage $I(V)\simeq D_F(E_F-eV)V$ by using the Tersoff-Hamann theory[42,43] for the $(dI/dV)/(I/V)-V$ curve. As a result, the $(dI/dV)/(I/V)-V$ curve is approximately expressed as $(dI/dV)/(I/V)\simeq 1+\{[dD(E_F-eV)/dV]/D(E_F-eV)\}V$ by carrying out the easy calculation. Accordingly, the slope of the $(dI/dV)/(I/V)-V$ curve at V corresponds to $[dD(E_F-eV)/dV]/D(E_F-eV)$. For the graphite surface and a Pt probe, $[dD(E_F-eV)/dV]/D(E_F-eV)\sim 1\ \text{V}^{-1}$ around the Fermi energy.[41] This means that $\bar{D}_s(E_F)/D_s(E_F)\sim 1\ \text{V}^{-1}$ for the graphite surface. Using this relationship, we can estimate the $C_{111}(d)$ curve. Figure 15(a) shows the $C_{111}(d)$ curve for $D_s=10^{-4}$ pF/nm^2 and $\bar{D}_s=10^{-4}$ pF/V nm^2. $\bar{D}_t$ at E_F is very small as assuming that the electric property of the probe tip is a metallic. Accordingly, $\bar{D}_t=10^{-8}$ pF/V nm^2 is used in the model calculations. The solid black line corresponds to the $C_{111}(d)$ curve obtained from Eq. (40). The solid red line corresponds to the $C_{111}^{\text{class}}(d)$ curve obtained from Eq. (41). The kink at $d\sim 0.7$ nm is recognized in the $C_{111}(d)$ curve. Below $d\sim 0.7$ nm, the $C_{111}(d)$ curve exponentially increases with decreasing d. This indicates the possibility that the $C_{111}(d)$ curve is similar to the AFM or STM approach curve. On the other hand, the

kink is not recognized in the $C_{111}^{\mathrm{class}}(d)$ curve, and a drastic increase occurs below $d \sim 0.1$ nm although $C_{111}^{\mathrm{class}}(d)$ is consistent with $C_{111}(d)$ above $d \sim 0.7$ nm. Furthermore, $C_{111}^{\mathrm{class}}(d)$ is smaller than $C_{111}(d)$ between $d=1$ and 0 nm.

Actually, NC-SNDM can indirectly detect the nonlinear capacitance due to the modulated resonance frequency reflected in the capacitance between the probe tip and metallic surface as described in the principle of NC-SNDM. Accordingly, we need to understand the relationship between the resonance frequency and total capacitance. As mentioned above, $C_g(d)$ and $C_{11}S_{11}$ are neglected in the total capacitance because $C'+C_{\mathrm{P\text{-}R}}$ is much larger than $C_g(d)$ and $C_{11}(d)S_{11}$ in the NC-SNDM measurement. Accordingly, substituting $C(V_A \sin(\omega t),d) \simeq C_{111}(d)S_{111}V_A \sin(\omega t)/2$ in Eq. (3), we obtain

$$\Omega_t(t,d) \simeq \frac{1}{\sqrt{L[C' + C_{\mathrm{P\text{-}R}} + C(t,d)]}}$$
$$= \Omega(d)\left\{1 - \sum_{l=1}^{\infty} \frac{\prod_{k=1}^{2l-1}(2k-1)}{2^{(2l-1)}(2l-1)!}\left[\frac{C_{111}(d)V_A S_{111}}{C' + C_{\mathrm{P\text{-}R}}}\right]^{2l-1} \times \sin(\omega t) + \sum_{l=1}^{\infty} \frac{\prod_{k=1}^{2l}(2k-1)}{2^{2l}(2l)!} \times \left[\frac{C_{111}(d)V_A S_{111}}{C' + C_{\mathrm{P\text{-}R}}}\right]^{2l} \cos(2\omega t) - \cdots\right\}, \quad (43)$$

where

$$\Omega(d) \equiv \frac{1}{\sqrt{L(C' + C_{\mathrm{P\text{-}R}})}} \quad (44)$$

and S_{111} is the effective square area for C_{111}. Accordingly, the $A_1(d)$ and $A_2(d)$ curves are

$$A_1(d) = |b_1(d)| = \left|\Omega(d)\sum_{l=1}^{\infty} \frac{\prod_{k=1}^{2l-1}(2k-1)}{2^{(l-1)}(2l-1)!}\left[\frac{C_{111}(d)V_A S_{111}}{C' + C_{\mathrm{P\text{-}R}}}\right]^{2l-1}\right|, \quad (45)$$

$$A_2(d) = |a_2(d)| = \left|\Omega(d)\sum_{l=1}^{\infty} \frac{\prod_{k=1}^{2l}(2k-1)}{2^{l}(2l)!}\left[\frac{C_{111}(d)V_A S_{111}}{C' + C_{\mathrm{P\text{-}R}}}\right]^{2l}\right|. \quad (46)$$

The $A_1(d)$ curve is expected to be larger than the $A_2(d)$ curve for a graphite surface if V_A is very small. Actually, the quality of the image for $A_2(d)$, which corresponds to the topography in Fig. 7(a), is considered to be poorer than that for $A_1(d)$ which is the ω amplitude image in Fig. 7(d). This indicates that the approximation described above to understand the origin of the capacitance in the graphite surface is almost satisfied. However, in order to understand the characteristics of the SNDM signals or images for the graphite surface in detail, it is necessary to theoretically investigate the relationship between the height of the probe tip and the SNDM signal. For this reason, we calculated $A_1(d)$, as shown in Fig. 15(b). We used $C'+C_{\mathrm{P\text{-}R}}=1.1\times10^{-3}$ pF which is obtained from the $\Omega(0,d)$ curve in Fig. 14(b). The effective square area for C_{111} is estimated to be $S_{111} \sim 0.01$ nm^2 at least due to the surface structure with ~ 0.1 nm in the graphite surface observed by NC-SNDM. The $A_1(d)$ curve is similar to the $C_{111}(d)$ curve as seen from Fig. 15(a). The reason for the $C_{111}(d)$ curve being consistent with the $A_1(d)$ curve is that $C_{111}V_A S_{111}$ is much smaller than $C'+C_{\mathrm{P\text{-}R}}$. As a result, the first term in $A_1(d)$ is the most dominant, and $A_1(d) \sim C_{111}(d)V_A$. Accordingly, $A_1(d)$ is much smaller than $\Omega_0(d)$. Actually, as seen from Figs. 7(c) and 15(b), the observed $A_1(d)$ is from ~ 100 Hz to ~ 1 kHz and corresponds to the calculated A_1 below $d < \sim 0.2$ nm. In the NC-SNDM measurement, d, which is the gap between the probe tip and the metallic surface, is estimated to be very small although the accuracy of the approximation in this model is poor. This means that it is necessary to bring the probe tip as close as possible to the surface to detect the graphite surface in the NC-SNDM measurement. Furthermore, we consider the function of the $A_1(d)$ curve. To compare another STM technique, the $e^{-d/l}/d$ curve, which is similar to the function expected from the approach curve for STM[44,45] is also plotted in Fig. 15(b). For $d<0.7$, the $A_1(d)$ curve is similar to the $e^{-d/l}/d$ curve. This means that the function of the signal distance for NC-SNDM for the small gap between the graphite and probe tip is considered to be similar to STM or AFM. Next, we discuss the resolutions for lateral and vertical directions in the NC-SNDM measurement. In the NC-SNDM measurement, the signal-to-noise ratios (k_1 and k_2) for the ω and 2ω amplitudes can be easily estimated from Fig. 7 as $k_1, k_2 \geq 1000$ since the resolution of the FM demodulator used in this study is almost ≤ 1 Hz. The vertical resolution can be estimated to be $\delta z \simeq l/k_i = 40$ fm from $(A_i - \delta A_i)/A_i = \exp(-\delta d/l) \simeq 1 - \delta d/l$ for $\delta d/l \ll 1$ due to $A_i \propto \exp(-d/l)$. The lateral resolution for the probe tip can be additionally estimated to be $\delta x \simeq (2a \times \delta d)^{-1/2} \simeq 3$ pm since the radius of the probe tip is $a \simeq 0.1$ nm corresponding to the size of a single atom of the probe tip. This indicates that NC-SNDM can also detect the atomic structure of the metallic surface. Thus, the origin of the signal observed by NC-SNDM is considered to be the electrochemical capacitance related to negative and positive carriers induced in the interface between the probe tip and the metallic surface by the applied voltage.

The $A_1(d)$ curves for various D_s and $\bar{D}_s$ are calculated to understand the A_1 obtained from the electrical properties of the region between the probe tip and the graphite surface in detail. Figure 16 shows various $A_1(d)$ curves for D_s and $\bar{D}_s$ from 10^{-7} to 10^{-2} pF/nm^2 and 10^{-7} to 10^{-2} pF/V nm^2. For $D_s=10^{-7}$ pF/nm^2 and $\bar{D}_s=10^{-7}$ pF/V nm^2, the peak is recognized to be at $d \sim 0.05$ nm. Above $d \sim 0.05$ nm, the $A_1(d)$ curve decreases. With increasing D_s and $\bar{D}_s$, the individual

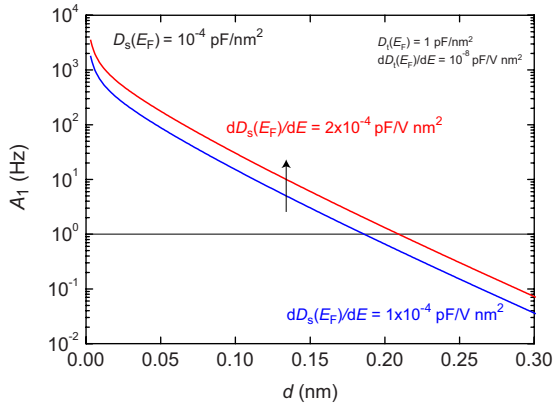

FIG. 17. (Color online) $A_1(d)$ curves with the quantum effect for $\bar{D}_s(E_F)=1\times10^{-4}$ pF/V nm^2 and 2×10^{-4} pF/V nm^2.

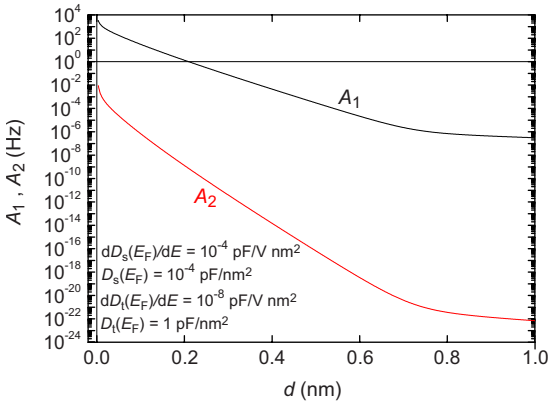

FIG. 18. (Color online) $A_1(d)$ and $A_2(d)$ curves with the quantum effect for various $D_s(E_F)=10^{-4}$ pF/nm^2 and $\bar{D}_s(E_F)=10^{-4}$ pF/V nm^2.

$A_1(d)$ curves are divided into two parts. The first is similar to the $A_1(d)$ curve for $D_s=10^{-7}$ pF/nm^2 and $\bar{D}_s=10^{-7}$ pF/V nm^2 above $d\sim0.05$ nm. However, the absolute of A_1 is smaller than that for $D_s=10^{-7}$ pF/nm^2 and $\bar{D}_t=10^{-7}$ pF/V nm^2. The $A_1(d)$ curve in this region corresponds to the classical contribution as seen from Fig. 15(b). Another is similar to the $e^{-d/l}/d$ curve. Focusing on the $A_1(d)$ curve for $D_s=10^{-4}$ pF/nm^2 and $\bar{D}_s=10^{-4}$ pF/V nm^2, we find that the $A_1(d)$ curve depends on $A_1(d)\propto e^{-d/l}/d$ below $d\sim0.7$ nm and is expressed as $A_1(d)=Ce^{-d/l}/d$, where C is a constant. A similar tendency is recognized in the $A_1(d)$ curves below $D_s=10^{-3}$ pF/nm^2 and $\bar{D}_s=10^{-3}$ pF/V nm^2 although the positions of the kink are different in all the curves.

The difference in the A_1 signals between the A and B sites on the graphite surface is considered. It should be remembered that the values of D_s and $\bar{D}_s$ were estimated from the $(dI/dV)/(I/V)-V$ curve for the Pt probe obtained from theory or STM observations.[41] The difference in the $(dI/dV)/(I/V)-V$ curve on the A and B sites is not considered in the above discussion, and the slope of $(dI/dV)/(I/V)$ at E_F is $\sim\bar{D}_s/D_s\sim1$ V^{-1}. However, the $(dI/dV)/(I/V)-V$ curves at A and B sites are different.[41] Actually, $\bar{D}_s/D_s$ for the A site is approximately twice $\bar{D}_s/D_s$ for the B site around $V\sim0$ V$(E\sim E_F)$.[41] Accordingly, $\bar{D}_s/D_s$ for the B site is set to 1/2 V^{-1}. Figure 17 shows the calculated $A_1(d)$ curves for $\bar{D}_s/D_s=1$ V^{-1} and 1/2 V^{-1}. $A_1(d)$ for $\bar{D}_s/D_s=1/2$ V^{-1} is approximately twice $A_1(d)$ for $\bar{D}_s/D_s=1$ V^{-1}. This relation is reflected in the experimental results in Fig. 7(d). Thus, we can understand that the principle of NC-SNDM is very similar to that of STM, and the tunneling effect is very important in both measurements.

Similar to the $A_1(d)$ curve, we can calculate the $A_2(d)$ curve from Eq. (46). Figure 18 shows the calculated $A_2(d)$ curve for $D_s=10^{-4}$ pF/nm^2 and $\bar{D}_s=10^{-4}$ pF/V nm^2. The $A_1(d)$ curve for $D_s=10^{-4}$ pF/nm^2 and $\bar{D}_s=10^{-4}$ pF/V nm^2 is also plotted in Fig. 18. The $A_2(d)$ curve is much smaller than the $A_1(d)$ curve. As described in the section on the principle of the SNDM, if $V_A=0.4$ $V_{p\text{-}p}$ can be estimated to be small, the $C_t(V)$ curve is approximately linear in the range of ±0.4 V, and $C_t[V_A\sin(\omega t),d]\simeq C_{P\text{-}R}+C_g(d)+C_{111}(d)S_{111}V_A\sin(\omega t)/2$ is considered to be appropriate. However, A_2 used in the NC-SNDM measurement is larger than the calculated A_2. For this reason, higher order capacitance greater than the second-order one is needed to be introduced in C_t to obtain A_2 used in the measurement. However, it is not easy to introduce the higher order capacitance in this paper due to the calculation of $d\bar{D}_s/dE=d^2D_s/dE^2$, which is obtained from the theoretical calculation.[33] We hope to carry out the calculation considering the higher order capacitance, greater than the second-order one, by using first-principles calculations in the future.

3. Current in NC-SNDM

The current image of the graphite surface in the NC-SNDM measurement is considered next. As mentioned above, the electrochemical capacitance originating from the band structure, as shown in Fig. 11, is crucially important to understand the origin of the SNDM signal for the metallic surface in the NC-SNDM measurement. Figure 11 also shows the band structures of the metallic surface and the probe tip for STM. By applying voltage to the specimen, a difference in the Fermi energies between the probe tip and the graphite surface occurs, and a tunneling current flows due to the applied voltage. Thus, as mentioned above, although we considered the electrochemical capacitance with the tunneling, this phenomenon is the same as that for STM. Therefore, it is considered that the current image in the NC-SNDM measurement reflects the tunneling effect between the probe tip and the graphite surface, and is similar to the SNDM image in the NC-SNDM measurement.

Next, we consider the relationship between the current image and the SNDM images. If the amplitude of the alternating voltage $[V(t)]$ used in this study is very small, the tunneling current can be expressed as $I(t)=I[V(t)]\sim D_s[E_F-eV(t)]V(t)=D_s[V(t)]V(t)$.[42,43,46] In this case, the local density of states for the graphite surface is approximately estimated to be

$$D_s(V) \sim \frac{dD_s(E_F)}{edV}(eV - E_F) + D_s(E_F)$$

$$= -\bar{D}_s(E_F)(eV - E_F) + D_s(E_F). \quad (47)$$

Substituting $V(t) = V_A \sin(\omega t)$ for $I[V(t)]$ and calculating the direct current component (I_0), we can obtain

$$I_0 \sim \frac{\omega}{2\pi}\int_{-\pi/\omega}^{\pi/\omega} I[V_A \sin(\omega t)]dt \sim -\frac{V_A}{2}\bar{D}_s(E_F). \quad (48)$$

Since C_{111} is approximated to $C_{111} \sim \bar{D}_s(E_F)$, as seen from Eq. (40) and as mentioned above, $I_0 \sim -V_A C_{111}(d)$. Therefore, I_0 is finally approximated to be $I_0 \sim A_1(d)$ because $A_1(d) \sim V_A C_{111}$ for the graphite surface as mentioned above. This means that I_0 is reflected in the ω amplitude signal observed by NC-SNDM $[A_1(d)]$.

The sign of I_0 is considered to be negative ($I_0 < 0$) because $\bar{D}_s(E_F) > 0$ as expected from the $dI/dV - V$ curve for 0 T for the graphite surface.[47] As a result, the $I(V)$ curve for the graphite surface is expected to approximately correspond to the case of $I^{(2)}(V)$ in Fig. 5(b). The expected sign of I_0 is consistent with the sign of the observed current signal, as seen from Fig. 8(f). This shows that the current observed in the NC-SNDM measurement ($I_0 < 0$) is reflected in the curvature of the $I(V)$ curve originating from the tunneling between the probe tip and the graphite surface. Thus, the NC-SNDM technique can detect not only the electrochemical capacitance but also transport by the quantum effect and provide significant information on the interface between the probe tip and graphite surface, as well as fullerenes, carbon nanotubes and organic molecules on a metallic surface.

V. CONCLUSIONS

We have observed clear SNDM images of graphite and Au(111) surfaces by using the NC-SNDM technique in an ultrahigh vacuum. The honeycomb structure formed from many hexagons was observed in the inverted contrast ω amplitude image as the probe tip was close to the graphite surface. A number of convex sites, with threefold symmetry, positioned at the corners of the hexagons were also observed in the inverted contrast ω amplitude image. On the other hand, a number of convex sites, with threefold symmetry, were also observed in the normal contrast ω amplitude image as the distance between the probe tip and the graphite surface became larger. The results suggest that the hollow in the ω amplitude image for the low position of the probe tip corresponds to the *A* site. In contrast, the convex in the ω amplitude image for the high position of the probe tip corresponds to the *B* site. Furthermore, current images modulated by the tunneling current were also observed in the NC-SNDM measurement and reflected in the variation of the LDOS by the applied alternating voltage. The current image thus was similar to the ω amplitude image in the NC-SNDM measurement.

The electrochemical capacitance between two metallic surfaces in a nanojunction was introduced to explain the origin of SNDM and current images. We succeeded in quantitatively showing that the ω amplitude signals in the graphite surface were reflected in the ratio of the slope of the LDOS on the graphite surface (D_s) and D_s. This suggests that not only STM and NC-AFM but also NC-SNDM techniques can detect LDOS in the graphite surface although the observation parameter utilized in the three techniques is different. Investigating the LDOS of the surface using the NC-SNDM technique is very important to not only observe the structure with atomic resolution but also to understand the properties in the interface between the probe tip and the graphite surface, providing a new point of view.

ACKNOWLEDGMENTS

We would like to acknowledge Masao Uno of Murata Manufacturing Co. Ltd. and Toshihiko Iwai of RIEC, Tohoku University, for supporting the development of the high-sensitivity SNDM probe.

*kshin@atom.che.tohoku.ac.jp

[1] Y. Cho, A. Kirihara, and T. Saeki, Rev. Sci. Instrum. **67**, 2297 (1996).
[2] Y. Cho, S. Kazuta, and K. Nakamura, Jpn. J. Appl. Phys. **36**, 3152 (1997).
[3] Y. Cho, S. Kazuta, and K. Matsuura, Appl. Phys. Lett. **75**, 2833 (1999).
[4] H. Odagawa and Y. Cho, Surf. Sci. **463**, L621 (2000).
[5] T. Morita and Y. Cho, Jpn. J. Appl. Phys. **45**, 4489 (2006).
[6] Y. Cho, Jpn. J. Appl. Phys. **46**, 4428 (2007).
[7] K. Tanaka, Y. Kurihashi, T. Uda, Y. Daimon, N. Odagawa, R. Hirose, Y. Hiranaga, and Y. Cho, Jpn. J. Appl. Phys. **47**, 3311 (2008).
[8] K. Honda, S. Hashimoto, and Y. Cho, Nanotechnology **16**, S90 (2005).
[9] K. Honda, S. Hashimoto, and Y. Cho, Nanotechnology **17**, S185 (2006).
[10] K. Ishikawa, K. Honda, and Y. Cho, Nanotechnology **18**, 084015 (2007).
[11] R. Hirose, K. Ohara, and Y. Cho, Nanotechnology **18**, 084014 (2007).
[12] Y. Cho and R. Hirose, Phys. Rev. Lett. **99**, 186101 (2007).
[13] S. Kobayashi, R. Hirose, and Y. Cho, J. Vac. Soc. Jpn. **51**, 771 (2008), in Japanese.
[14] S. Kobayashi, R. Hirose, and Y. Cho, J. Vac. Sci. Technol. B **28**, C4D18 (2010).
[15] P. Mallet, F. Varchon, C. Naud, L. Magaud, C. Berger, and J.-Y. Veuillen, Phys. Rev. B **76**, 041403 (2007).
[16] K. S. Novoselov, A. K. Geim, S. V. Morozov, D. Jiang, Y. Zhang, S. V. Dubonos, I. V. Grigorieva, and A. A. Firsov, Science **306**, 666 (2004).
[17] K. S. Novoselov, A. K. Geim, S. V. Morozov, D. Jiang, M. I.

Katsnelson, S. V. Dubonos, I. V. Grigorieva, and A. A. Firsov, Nature (London) **438**, 197 (2005).
[18] Y. Zhang, Y.-W. Tan, H. L. Stormer, and P. Kim, Nature (London) **438**, 201 (2005).
[19] D. Tománek and S. G. Louie, Phys. Rev. B **37**, 8327 (1988).
[20] D. Tománek, S. G. Louie, H. J. Mamin, D. W. Abraham, R. E. Thomson, E. Ganz, and J. Clarke, Phys. Rev. B **35**, 7790 (1987).
[21] H. A. Mizes, S. I. Park, and W. A. Harrison, Phys. Rev. B **36**, 4491 (1987).
[22] S. Park and C. F. Quate, Appl. Phys. Lett. **48**, 112 (1986).
[23] F. Atamny, O. Spillecke, and R. Schlogl, Phys. Chem. Chem. Phys. **1**, 4113 (1999).
[24] N. Kin, R. Hirose, and Y. Cho, J. Vac. Sci. Technol. B **28**, C4D5 (2010) .
[25] N. Kin, R. Hirose, and Y. Cho, J. Appl. Phys. **107**, 104121 (2010).
[26] J. G. Hou, Jinlong Yang, Haiqian Wang, Qunxiang Li, Changgan Zeng, Hai Lin, Wang Bing, D. M. Chen, and Qingshi Zhu, Phys. Rev. Lett. **83**, 3001 (1999).
[27] M. Buttiker, J. Phys.: Condens. Matter **5**, 9361 (1993).
[28] M. Büttiker, H. Thomas, and A. Prêtre, Phys. Lett. A **180**, 364 (1993).
[29] T. Christen and M. Buttiker, Phys. Rev. Lett. **77**, 143 (1996).
[30] K. Watanabe, S. Watanabe, M. Tanaka, and N. Nakaoka, Jpn. J. Appl. Phys. **44**, 5348 (2005).
[31] M. Tanaka, Y. Gohda, S. Furuta, and S. Watanabe, Jpn. J. Appl. Phys. **42**, L766 (2003).
[32] J. Wang, H. Guo, J.-L. Mozos, C. C. Wan, G. Taraschi, and Q. Zheng, Phys. Rev. Lett. **80**, 4277 (1998).
[33] X. Zhao, J. Wang, and H. Guo, Phys. Rev. B **60**, 16730 (1999).
[34] B. Wang, X. Zhao, J. Wang, and H. Guo, Appl. Phys. Lett. **74**, 2887 (1999).
[35] V. Gasparian, T. Christen, and M. Buttiker, Phys. Rev. A **54**, 4022 (1996).
[36] Y. Koguchi, T. Meguro, A. Hida, H. Takai, K. Maeda, Y. Yamamoto, and Y. Aoyagi, Nucl. Instrum. Methods Phys. Res. B **206**, 202 (2003).
[37] H. Hashimoto, M. Watanabe, S. Nishiuma, K. Nakamura, and S. Yoshida, Surf. Interface Anal. **35**, 19 (2003).
[38] J. Robertson, J. Vac. Sci. Technol. B **17**, 659 (1999).
[39] G. Rietveld, N. Y. Chen, and D. van der Marel, Phys. Rev. Lett. **69**, 2578 (1992).
[40] D. Purdie, H. Bernhoff, and B. Reihl, Surf. Sci. **364**, 279 (1996).
[41] N. Isshiki, K. Kobayashi, and M. Tukada, J. Vac. Sci. Technol. B **9**, 475 (1991).
[42] J. Tersoff and D. R. Hamann, Phys. Rev. Lett. **50**, 1998 (1983).
[43] J. Tersoff and D. R. Hamann, Phys. Rev. B **31**, 805 (1985).
[44] R. H. Fowler and L. Nordheim, Proc. R. Soc. London, Ser. A **119**, 173 (1928).
[45] R. D. Young, J. Ward, and F. Scire, Phys. Rev. Lett. **27**, 922 (1971).
[46] A. Selloni, P. Carnevali, E. Tosatti, and C. D. Chen, Phys. Rev. B **31**, 2602 (1985).
[47] T. Matsui, H. Kambara, Y. Niimi, K. Tagami, M. Tsukada, and H. Fukuyama, Phys. Rev. Lett. **94**, 226403 (2005).